Atomistic simulation and interatomic potential comparison in α-Al 2 O 3 : lattice, surface and extended-defects properties

Qinqin Xu, Nicolas Salles, Jérome Chevalier, Jonathan Amodeo

Atomistic simulation and interatomic potential comparison in α-Al_2O_3: lattice, surface and extended-defects properties

Qinqin Xu[1], Nicolas Salles[2], Jérome Chevalier [1] and Jonathan Amodeo[1,3]

[1] Univ Lyon, CNRS, INSA Lyon, UCBL, MATEIS, UMR5510, 69621 Villeurbanne, France

[2] CNR-IOM/Democritos National Simulation Center, Istituto Officina dei Materiali, c/o SISSA, via Bonomea 265, IT-34136 Trieste, Italy

[3] Aix-Marseille Univ, Université de Toulon, CNRS, IM2NP, Marseille, France

E-mail: jonathan.amodeo@insa-lyon.fr

Abstract. Aluminum oxide (α-Al_2O_3) is known as one of the major ceramic oxide and is currently used for its advanced mechanical properties. Nowadays, it requires a more in-depth description at small-scales especially for applications in the fields of nanocrystalline ceramic fabrication and nanomechanics. In this study, we investigate the transferability of several types of interatomic potentials including rigid ion, 2/3-body and many body variable charge models. In particular, a special attention is paid to the material properties that are the more relevant for nanomechanical applications such as lattice properties, surface and stacking fault energies as well as dislocation modeling. Simulation outcomes are compared to reliable DFT simulations and most up-to-date experiments available from the literature.

1. Introduction

Hereafter its main role as the most important aluminum precursor, α-alumina (α-Al_2O_3) is one of the top-known ceramics used for its excellent mechanical properties in various fields of application such as abrasives [1, 2], catalysis [3, 4] and medical engineering [5, 6]. Since the pioneer work of Boutin, it is one of the main materials used for hip replacement due to its high bio-compatibility [7, 8, 9]. It is also commonly used for dental brackets and crowns [10, 11]. However, alumina compounds are generally constrained to be thick to compensate their lack of toughness.

Thus, various strategies are adopted to improve the mechanical properties of alumina-based materials. Al_2O_3 is regularly combined to other metal oxides such as zirconia (ZrO_2), ceria (CeO_2) or titania (TiO_2) to build alloys and composites with enhanced mechanical properties [12, 13, 14, 6, 15, 16]. A significant effort is also conducted to refine the starting-powder size and target alumina-based nanocrystalline alloys [17]. Along

that line and to improve the understanding of nanoscale alumina mechanical properties, Calvie *et al.* performed *in-situ* TEM nanocompression tests of alumina nanoparticles which are commonly used for the process of bulk pieces [18, 19]. The authors emphasize the unprecedented ductility reached by the individual alumina nanocrystal although they do not conclude about the elementary mechanisms responsible for such a peculiar behaviour. Indeed, while reducing the size of single-crystalline ceramics deep in the submicron scale is known to promote a brittle-to-ductile transition and postpone (or inhibit) the fracture process [20, 21, 19, 22, 23, 24, 25], few is known about the influence of size on the plastic deformation mechanisms.

To address this issue, molecular dynamics (MD) simulations are regularly used to supplement experimental studies at small-scale. In particular, these simulations are currently applied to investigate the deformation processes of single- and nanocrystalline structures [26, 27].

Sarobol *et al.* investigated the plasticity of defective and defect-scarce alumina micro- and nanoparticles using room temperature *in-situ* TEM compression tests and MD simulations [28]. For single-crystalline nanoparticles with compression axis along [0001], the authors observed dislocation nucleation from the contact area between the indenter and the sample within the rhombohedral slip system. The authors have shown that the nanoparticles fracture into separated parts after that a significant amount of deformation was reached. For bicrystalline particles, atom reshuffling is observed first at the contact between the indent and the grain boundary before voids appear promoting the bicrystal fracture. No dislocation nucleation was observed in the simulation of bicrystals. Zhang *et al.* studied the deformation mechanisms of α-alumina thin films using impact loading MD simulations [29]. Analysis of inner impact faces have shown wild deformation patterns (just below the impact) with dislocations nucleation events. Various slip systems and deformation processes typical of the alumina crystalline structure were identified including basal, prismatic and pyramidal slip as well as basal and rhombohedral twinning. New deformation processes including twinning in $\{0\bar{1}11\}$ were also identified probably due to the specific impact conditions of deformation. A similarly complex plastic behaviour was emphasized by Nishimura *et al.* using nanoindentation MD simulations [30].

In the simulation, the elementary deformation processes believed to be responsible of nanoscale α-alumina deformation seem more extensive than those of the classical picture inferred from high-temperature bulk experiments [31, 32, 33]. However, conclusions have to be drawn with care when exclusively derived from MD simulations as those are known to be particularly dependent on the interatomic potential used.

Indeed, interatomic potentials are the crucial ingredient of atomistic simulations *i.e.*, they integrate all the theoretical background and the physical hypothesis made to compute the energy and derive the interatomic forces of the investigated system. For each class of materials, specific frameworks often derived from the quantum theory were developed to better reflect the physics of the atomic bond with more or less complexity. For example in metal oxides, one of the simplest (and most used) interatomic model

is the original rigid ion (RI) model [34]. The RI formulation assumes non-deformable ions with fixed charges ruled by short range (buckingham) and coulombic interactions. An other kind of theoretical framework developed to model metal oxides is 2/3-body potentials as proposed by Vashishta *et al.* [35, 36, 37]. These potentials are inspired from the Stillinger-Weber formalism originally developed to model covalent materials as silicon [38, 39]. Indeed, the ionic *vs.* covalent bivalence of the atomic bond in oxides is often modeled using either ionic original RI models (Buckingham) or Stillinger-Weber like potentials including an angular interaction term. Nevertheless, while these methods allow for large-scale simulations they often suffer from their intrinsic simplicity leading to the development of more complex variable charge models including the ReaxFF [40], the COMB3 [41, 42] and the SMTB-Q formalisms [43, 44].

Most of the aforementioned formalisms were more or less recently adjusted to model α-Al_2O_3 properties. In this study, after a reminder about interatomic potential theoretical aspects, we will test and compare the transferability of a large bench of RI, 2/3-body and variable charge potentials. A special attention will be paid to the characterization of material properties that are significant for nanomechanical applications including not only lattice and elastic properties but also surface and stacking fault energies as well as dislocation properties. The pros and cons of each potential will be discussed all along the study shading light on the best compromise to be done to target larger-scale nanomechanical simulations.

2. Interatomic potentials: theoretical framework and parameterization

In this study, we investigate the transferability of α-Al_2O_3 interatomic potentials to lattice and dislocation properties using atomistic simulations and the LAMMPS code [45]. Three types of interatomic potentials are investigated namely the RI formalism relying on Buckingham potentials [34, 46, 47, 48] , the 2/3-body interaction potentials [49, 50] and the variable charge SMTB-Q potential [44].

The general formulation of RI potentials is recalled in Equation 1. The first two terms rely on short-range interactions. They are known as Buckingham potential [51] and includes the Pauli exclusion principle and van der Waals interactions, while the third term is the long-range Coulombic interaction characterized by the atom pair ionic charges q_i and q_j.

$$V_{ij}(r_{ij}) = A_{ij}exp(\frac{-r_{ij}}{\rho_{ij}}) - \frac{C_{ij}}{r_{ij}^6} + \frac{q_i q_j}{4\pi\varepsilon_0 r_{ij}} \quad (1)$$

where A_{ij}, ρ_{ij} and C_{ij} are the fitting parameters and r_{ij} is the distance between ij pairs of ions.

RI potentials are fixed charged potentials *i.e.,* a constant charge is associated to each ion during the whole simulation run. This net charge can be different from the theoretical (or experimental) one and is often integrated in the fitting procedure. In this study, short-range interactions are computed in the real space for $r_{ij}<r_c$, with r_c the short-range cutoff radius. In the following, we use the largest r_c=12 Å for each RI parameterization investigated. On the other hand, long-range interactions are computed using Ewald [52] (with long-range radius r_s=r_c), Wolf [53]) or the muti-level summation method (MSM) [54] depending on both the investigated problem and the formalism used. More details about charge summation will be provided later.
Here we investigate four different RI parameterizations including those of Bush without the shell contribution [47], Catlow [34], Gale [46] and Sun [48]. Potential parameters are provided in table 1.

		Bush	**Catlow**	**Gale**	**Sun**
Al-O	A(eV)	2409.505	1460.3	3596.94	3411.118
	ρ(Å)	0.2649	0.29912	0.23650	0.244549
	C(eV.Å^6)				
O-O	A(eV)	25.41	22764.3	435.63	91.55955
	ρ(Å)	0.6937	0.1490	0.36070	0.547148
	C(eV.Å^6)	32.32	27.879	0.49	32.32
Al-Al	A(eV)			9830.51	
	ρ(Å)			0.28870	
	C(eV.Å^6)			675.70	
Al^{+q} (e)		3	3	2.25	3
O^{-q} (e)		2	2	1.5	2

Table 1. RI potential parameters from Bush *et al.* [47], Catlow *et al.* [34], Gale *et al.* [46] and Sun *et al.* [48].

In the Catlow potential [34], short-range interaction parameters are derived from experimental lattice and elastic constants, dielectric constants, cohesive energy using least-squares fitting routine. The O-O interaction is taken from [55], Al-Al interactions are purely coulombic and the short-range attractive r^{-6} interaction is ignored for Al-O (the latter being adopted in every RI parameterizations discussed here). Catlow potentials are the root of fully-ionic models and were originally developed to investigate cohesive, elastic and lattice dynamics properties of oxides and halides. The parameters of the Gale potential (Mulliken reference 3) are obtained using a periodic *ab initio* Hartree-Fock method applied to energy hypersurface [46]. In addition, they used the Mulliken energy obtained at the minimum energy conformation to set partial charge values. The Al charge changes up to 0.3e due to lattice distortion leading to electrostatic energy variations included into the short-range interaction term. The Bush potential is fitted using various crystal structures, relative permitivities and elastic constants for a

large set of metal compounds [47]. In Bush study, all fitting procedures are performed with the General Utility Lattice Program (GULP) [56]. The Sun potential [48] relies on a simplified version of the original Matsui model [57] built to investigate crystal structures and bulk moduli of CaO-MgO-Al_2O_3-SiO_2 systems. After analytical simplifications, the authors readjusted the potential also using the GULP code. One can note that the authors biased the weighting factors strongly toward the lattice parameters at the expense of the elastic constants. The lattice energy was also included in the fitting procedure (but with a low weight). Their results show that neither the van der Waals terms involving cations nor the short-range cation–cation interactions need to be included in the simulations in order to obtain an acceptable reproduction of the experimental data.

Vashishta *et al.* proposed a 2/3-body interatomic parameterization that can be used for Al_2O_3 [50]. In comparison to the original RI model, the 2/3-body potentials generally better accounts for directional (covalent) features thanks to an angular term. The Branicio formulation [37] of the Vashishta potential used here is reminded in Equation 2.

$$V_{ijk}(r_{ij}, r_{ik}, \theta_{ijk}) = \sum_{i}^{N}\sum_{j>i}^{N} V_{ij}^{(2)}(r_{ij}) + \sum_{i}^{N}\sum_{j\neq i}^{N}\sum_{k>j,k\neq i}^{N} V_{ijk}^{(3)}(r_{ij}, r_{ik}, \theta_{ijk}) \tag{2}$$

where N is the total number of atoms and θ_{ijk} is the angle formed by $\overrightarrow{r_{ij}}$ and $\overrightarrow{r_{ik}}$, relative position vectors between atoms i, j and k.

On one hand, the two-body term $V_{ij}^{(2)}(r_{ij})$ includes steric-size effects, charge-induced dipole, Coulomb and van der Waals interactions (Equation 3). It is applied here up to a cutoff distance r_c= 6 Å as in the original study.

$$V_{ij}^{(2)}(r_{ij}) = \frac{H_{ij}}{r_{ij}^{\eta_{ij}}} + \frac{q_i q_j}{r_{ij}} e^{(-r_{ij}/\lambda_{1,ij})} - \frac{D_{ij}}{r_{ij}^4} e^{(-r_{ij}/\lambda_{4,ij})} - \frac{W_{ij}}{r_{ij}^6}, r_{ij} < r_c \tag{3}$$

where H_{ij} and η_{ij} are respectively the strength and the size exponent of the steric repulsion, λ_1 and λ_4 are the screening lengths of the Coulomb and the charge-induced dipole interactions, respectively. D_{ij} and W_{ij} refer to the strengths of both the charge-induced dipole and the van der Walls interactions.

On the other hand, the 3-body term $V_{ijk}^{(3)}(r_{ij}, r_{ik}, \theta_{ijk})$ described in Equation 4 relies on the angular interaction between Al-O-Al and O-Al-O triplets of atoms. It is applied up to a cutoff distance r_0=2.9 Å.

$$V_{ijk}^{(3)}(r_{ij}, r_{ik}, \theta_{ijk}) = B_{ijk} \frac{\left[\cos\theta_{ijk} - \cos\bar{\theta}_{ijk}\right]^2}{1 + C_{ijk}\left[\cos\theta_{ijk} - \cos\bar{\theta}_{ijk}\right]^2} \times e^{\frac{\gamma}{r_{ij}-r_0}} e^{\frac{\gamma}{r_{ik}-r_0}}, r_{ij} \leq r_0, r_{ik} \leq r_0 \tag{4}$$

where B_{ijk} is the amplitude of the 3-body interaction and $\bar{\theta}_{ijk}$, C_{ijk} and γ are parameters of the 3-body interaction.

	Al	**O**	
q(e)	+1.5237	-1.0158	
	Al-Al	**Al-O**	**O-O**
λ_1(Å)		5.0	
λ_4(Å)		3.75	
r_c(Å)		6.0	
η_{ij}	7.0	9.0	7.0
H_{ij}(eV.Å$^\eta$)	12.7506	249.3108	564.7334
D_{ij}(eV.Å^4)	0.0	25.076	22.290
W_{ij}(eV.Å^6)	0.0	0.0	79.2884
r_c(Å)	6.0	6.0	6.0
	Al-O-Al	**O-Al-O**	
B_{ijk}(eV)	8.1149	12.4844	
cos($\bar{\theta}_{ijk}$)	-0.33331	0.0	
γ(Å)	1.0	1.0	
r_0(Å)	2.90	2.90	
C_{ijk}	10.0	10.0	

Table 2. Al_2O_3 parameters of Vashishta 2/3-body interatomic potential [50].

The many-body SMTB-Q interatomic potential is a variable charge model originally developed by Tétot [58, 59]. It is based on the charge equilibration QEq method that allows for local ionic charge variations using the electronegativity equalization principle of Rappé *et al.* [60]. While it is the most complex formulation used in this study, it is also the closest to the quantum theory as it allows for the *on-the-fly* evaluation of the ionic charge [61]. As emphasized by Salles and collaborators, the SMTB-Q potential is particularly suited to model α-Al_2O_3 properties such as elastic constants, energy and atomic relaxation of surfaces. Moreover, this potential shows a reasonable description of various polymorphs of alumina [44]. This, however, at the expense of increased cpu costs when compared to the RI and 2/3-body formalisms what constrains its usage to small-scale MD simulations only (see the example benchmark in the supplementary information). Thus, the many-body SMTB-Q formalism will be used here mostly as a reference to confront the outcomes from RI and 2/3-body potentials together with DFT and experimental literature data. For these reasons, the SMTB-Q potential will be the only variable charge potential investigated here. Moreover, the SMTB-Q model was also used to investigate lattice and mechanical properties of UO_2, $SrTiO_3$ and TiO_2 often in agreement with experimental data [62, 63, 64, 65].

Within the many-body SMTB-Q approach, the potential energy can be described as

follows:

$$E_{coh} = E_{ion} + E_{coul} + E_{cov} + E_{rep} \tag{5}$$

with

$$E_{ion} = \sum \left(E_i^0 + \chi_i^0 q_i + 1/2 J_{ii}^0 q_i^2 \right) \tag{6}$$

$$E_{coul} = \sum_i \sum_{i<j} q_i q_j J_{ij} \tag{7}$$

$$E_{cov}^{i,j(i,j=Al,O)} = -\sum \left\{ \sum_{r_{ij} \leq r_c} \epsilon_i^2 exp \left[-2\zeta (\frac{r_{ij}}{r_0} - 1) \right] \Delta q_i \right\}^{1/2} \tag{8}$$

$$\begin{aligned} E_{rep}^{i,j(i,j=Al,O)} = & \sum_{r_{ij} \leq r_c}^{i} \sum_{r_{ji} \leq r_c}^{j} A_{ij} exp \left[-p_{Al} (\frac{r_{ij}}{r_0}) - 1 \right] (Al - O) \\ & + 1/2 \sum^{j} \sum_{r_{jj} \leq r_c}^{j} B exp(\frac{r_{jj}}{\rho}) (O - O) \end{aligned} \tag{9}$$

where E_{ion} is the second order ionization energy of the atom i defined using the neutral atom energy E_i^0, the electronegativity χ_i^O and the hardness J_{ii}^O, respectively. E_{coul} is the electrostatic term with J_{ij} the coulomb integral computed using two s-type Slater orbitals and the Wolf summation method (see Refs.[60, 53] for more details). E_{cov} is a covalent energy term that applies up to the second moment radius r_c^{2nd} located between the 4^{th} and 5^{th} neighbors of each Al and O atom [61]. ϵ_i and ζ are the hopping integral adjustable parameters (see Ref. [59] for more details). Δq_i refers to the covalent contribution of the delocalized electronic charges. Finally, E_{rep} is a short-range repulsive term made of Buckingham and Born-Mayer terms respectively for O-O and Al-O interactions (p_{Al} and B are adjustable parameters). Cation–cation short-range interactions are neglected. Parameters for a recently updated SMTB-Q interatomic potential are provided in Table 3. One can notice that the ReaxFF formalism was also parameterized for α-Al_2O_3 surface application with flawed transferability as shown in Ref. [66, 67]. Its transferability will not be detailed further in this study.

3. Calculation of lattice and surface properties

3.1. Unit cell, lattice parameters and elastic constants

α-Al_2O_3 is a iono-covalent ceramic ($R\bar{3}c$ space group) often described by a 30 atoms hexagonal unit cell with lattice parameters a_0=4.76 Å and c_0=12.99 Å [68]. In this study, an orthorombic unit cell made of 60 atoms is used for modeling convenience. It is characterised by cell vectors of lengths $a = a_0$, $b = \sqrt{3}a_0$ and $c = c_0$. Both unit cells

χ^0_O (eV)	6.57	ϵ_{Al} (eV)	0.7096
J^0_{OO} (eV)	10.22	ζ	1.5885
χ^0_{Al} (eV)	1.19	A_{ij} (eV)	0.1818
χ^0_{AlAl} (eV)	11.19	p_{Al} (eV)	8.8004
R_O (Å)	0.529	r_0 (Å)	1.91
R_{Al} (Å)	0.566	B (eV)	580.44
ϵ_O (eV)	0.5794	ρ (Å)	0.354

Table 3. Parameters of the many-body SMTB-Q interatomic potential for Al_2O_3 [44].

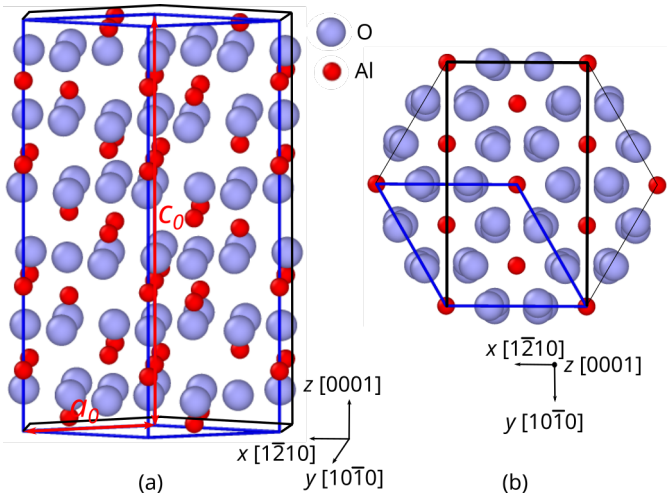

Figure 1. Crystal structure of α-Al_2O_3 (a) Perspective 3D view, (b) Projected view along the [0001] direction. The blue and black lines refer to the hexagonal (30 atoms) and orthorombic (60 atoms) cells, respectively.

are shown Figure 1.

A 3×3×3 orthogonal supercell is designed for the calculation of α-Al_2O_3 lattice parameters using periodic boundary conditions (PBCs). Firstly, the conjugate gradient method is used to minimize the potential energy of the system. A minimization stopping criterion of 10^{-4} eV/Å is applied on resulting net forces (whatever the interatomic potential used). Secondly, an anisotropic relaxation is performed down to zero pressure changing box dimensions and remapping atoms positions. Finally, the energy and resulting forces of the system are further minimized (without box relaxation) using the FIRE algorithm [69] down to a net force of 10^{-6} eV/Å for RI and 2/3-body interatomic potentials and 10^{-4} eV/Å for SMTB-Q. Results computed for the different interatomic potentials as compared to experimental and DFT data are presented in Table 4.

The elastic constants C_{ij} characterize the stiffness of a material. They link stress and strain tensors via the generalised Hooke's law $\sigma_i = C_{ij}\epsilon_j$. The α-Al_2O_3 stiffness matrix is defined by six independent elastic constants due to its hcp crystal symmetry.

Interatomic potential		**Lattice parameter (Å)**	
		a_0	c_0
Rigid ion	Bush	4.82 (4.82[47, 48])	13.01 (13.01[47, 48])
	Catlow	4.78 (4.78[46])	12.57 (12.53[46])
	Gale	4.76 (4.80[46], 4.79[70])	12.99 (12.94[46], 12.83[70])
	Sun	4.77 (4.77[48])	12.99 (12.99[48])
2/3-body	Vashishta	4.72	13.17
Variable charge	SMTB-Q	4.81 (4.79[44])	13.06 (13.06[44])
DFT			
Ref.[71, 72]		4.75±0.06	13.05±0.15
Experiment			
Ref.[73, 74]		4.75±0.01	12.99±0.01

Table 4. α-Al_2O_3 lattice parameters a_0 and c_0 computed at 0K using Bush [47], Catlow [34], Gale [46] and Sun [48] RI, Vashishta 2/3-body [50] and SMTB-Q [44] interatomic potentials. DFT [71, 72] and room temperature experiments [73, 74] data are shown for comparison.

Interatomic potential		**Elastic constants (GPa)**					
		C_{11}	C_{12}	C_{13}	C_{14}	C_{33}	C_{44}
Rigid ion	Bush	662.2 (607.2[47])	271.9 (322.2[47])	180.7	59.6	608.9 (606.5[47])	132.8 (95.3[47])
	Catlow	675.5 (648.5[46])	272.6 (293.1[46])	206.6 (207.7[46])	47.5 (42.2[46])	505.4 (490.8[46])	180.1 (162.3[46])
	Gale	560.3 (549.4[46])	263.6 (247.0[46])	220.4 (209.4[46])	17.3 (17.0[46])	460.6 (445.8[46])	170.0 (163.9[46])
	Sun	714.5 (714.5 [48])	327.6 (327.5[48])	187.8 (187.8[48])	69.1	709.3 (709.3[48])	99.7 (99.7[48])
2/3-body	Vashsishta	476.1 (523.0[50])	155.4 (147.0[50])	135.4 (129.0[50])	10.4 (7.5[50])	414.9 (427.0[50])	149.1 (135.0[50])
Variable charge	SMTB-Q	498.9 (607.0[44])	202.2 (134.0[44])	152.0 (145.0[44])	37.9 (181.0[44])	457.4 (486.0[44])	115.0 (164.0[44])
DFT							
Ref.[75, 76, 77]		515.7±22.3	169.2±10.8	117.5±12	16.2±4.8	510.2±14.8	161.1±5.9
Experiment							
Ref.[78, 79, 80]		497.3±0.2	162.8±0.2	116.2±0.8	22.4±0.3	501.8±1.5	147.2±0.2

Table 5. α-Al_2O_3 elastic constants computed at 0K using RI [34, 46, 47, 48], 2/3-body [50] and SMTB-Q [44] interatomic potentials as compared to litterature data. Room temperature experimental data from Ref. [78, 79, 80] and DFT simulation data from Ref. [75, 76, 77] are shown for comparison.

Elastic constants at 0K are easily computed combining a set of elementary deformation simulations and the generalised Hooke's law. For this purpose, a relaxed 3×3×3 supercell is iteratively deformed along all directions using PBCs. Stress response variations are computed after minimisation of the energy using the FIRE algorithm and a similar convergence criterion than aforementioned. Results are presented in Table 5.

Table 4 shows that all the interatomic potentials tested reproduce quite well the lattice parameters a_0 and c_0 when compared to DFT and experiments, except the Catlow RI potential that underestimates c_0 (12.56 Å when compared to average values 13.05 Å and 12.99 Å respectively for DFT and experiments). Results are more critical for elastic constants calculations as shown Table 5, where RI Bush, Catlow and Sun potentials are particularly off when compared to literature data. Indeed, RI potentials are not accurate enough here, except for the Gale potential which provides slightly better

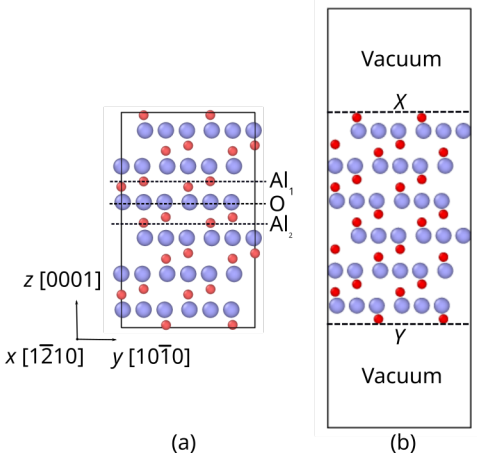

Figure 2. Slab-type supercell for basal surface energy calculation in α-alumina. The simulation relies on a collumnar supercell of Al_2O_3 oriented along the [0001] direction. Red and blue atom refers respectively to aluminum and oxygen atoms. O, Al_1 and Al_2 layers are depicted by dashed lines. (a) Original supercell used for E_{bulk} calculation. (b) Supercell with vacuum out of X=Al_2 and Y=Al_1 free surfaces.

results. On the other hand, 2/3-body Vashishta and SMTB-Q potentials provide more comparable results. On this basis, we conclude that the RI Gale [46], the 2/3-body Vashishta [50] and the SMTB-Q [44] interatomic potentials are particularly suited to describe α-Al_2O_3 lattice properties. A particular attention is paid to these three potentials in the following.

3.2. Surface energy

α-alumina surfaces have attracted a significant attention with applications in the field of catalysis, coating and electronics [81, 82, 83]. First-principle simulations show a specific surface energy ranking with $(0001) < \left\{1\bar{1}02\right\} < \left\{11\bar{2}0\right\} < \left\{10\bar{1}0\right\} < \left\{10\bar{1}1\right\}$ that emphasizes the higher stability of the basal (0001) surface [84, 85]. As shown Figure 2, the [0001] stacking of bulk α-Al_2O_3 can be described using the following simplified sequence ..-Al_2-O-Al_1-Al_2-O-.. with O a pure oxygen layer and Al_1 and Al_2 two consecutive aluminum layers shifted from each other. In the simulation, these three layers are often considered as first guesses to compute the (0001) surface energy. Guenard *et al.* have investigated the (0001) surface of α-alumina with single Al-terminated surface using grazing incidence X-ray scattering [86]. They conclude that the Al-terminated layer is closer to the underlying O layer due to surface relaxation when compared to bulk conditions. This result was confirmed by many low-energy electron diffraction studies [87, 88, 89]. DFT simulations show that the Al-terminated surface has the lowest surface energy at 0K [90]. A study of the effect of chemical potential of constituting elements on the surface energy shows that a Al-rich atmosphere promotes the Al-terminaison surface while the O-rich atmosphere favoured the O-terminaison surface [91]. Wang and

collaborators emphasize the role of a realistic environment containing both O and H species computing the Gibbs free energy to obtain theoretical predictions of the (0001) surface in agreement with experiments [92]. Blonski and collaborators performed molecular static simulations for the three possible surface terminations *i.e.*, the single O- and the two Al-terminated. After energy minimisation, the authors have shown similar results for the two Al-terminated surfaces including surface energies lower that in the O-terminated case [49]. For more details about (0001) surface energies computed in α-Al_2O_3, the reader can refer to the detailed literature review published in Ref. [66].

Generally, atomistic simulations of surface energy rely on supercell with either 3D-PBCs with empty space out of the surface of interest (see Figure 2) or free-BCs along this latter altogether with 2D-PBCs for the two in-plane perpendicular directions [93, 94, 95]. Whatever the simulation setup, the surface energy γ_s^{XY} can be derived using Equation 10,

$$\gamma_s^{XY} = \frac{E_{XY} - nE_{bulk}}{2A} \tag{10}$$

where E_{XY} is the minimized potential energy of the simulation cell including XY-terminated surfaces, E_{bulk} is the per-atom minimised energy of the bulk crystal, n is the number of atoms contained in the simulation cell and A is the cross-section area.

In simple structures (*e.g.*, fcc monoatomic metals), the two opposite side surfaces of a simulation supercell are the same (X=Y) what makes the surface energy calculation straightforward. However, surfaces can be hetero-terminated ($X \neq Y$) in more complex cases when the crystal structure is defined by plan changeovers along the surface stacking direction. In this case, the surface energy can be averaged (γ_s^{ave}) accounting for the two different surfaces (as *e.g*, in the case of $L1_2$ crystal {100} surface energy). In α-alumina, most of the crystallographic planes switch with a period larger than two what makes the definition γ_s^{ave} more complex. Obviously, one could force X=Y slicing the simulation supercell whatever the crystalline structure. However, this generally leads to non-stoichiometric configurations in ionic materials that are out of reach for most of classical charge summation algorithms.

In this study, we design slab simulations that refer to the three possible terminations of the (0001) surface *i.e.*, XY=Al_1O, Al_1Al_2 or OAl_2 (see Figure 3a and b) in order to solve a derived set of surface energy equations. At this stage, one can anticipate that Al_1O and OAl_2 surface energy simulations should lead to similar results as both Al basal surface terminations rely on the same atomic arrangement only shifted one from the other. However, it is preferred to keep both for a sake of clarity. Supercells are made out of $3\times3\times n_z$ unit cells. First, the simulation cell is relaxed using 3D-PBCs to compute E_{bulk} using the same energy minimization protocol than aforementioned (see lattice parameters method section), then the box dimension is extended twice along the

[0001] direction (without remapping atomic positions) to introduce vacuum and compute E_{XY} using the same minimization protocol and 3D-PBCs, as illustrated Figure 2. The Ewald, Wolf and MSM charge summation methods are tested in the case of the RI Gale interatomic potential. Long-range radius varying from 12 to 24 Å were tested for RI without significant changes on the conclusions and a relative accuracy of 10^{-6} was set for both Ewald and MSM. n_z values ranging from 3 to 21 were checked to quantify periodic electrostatic interactions between free-surfaces also without significant impacts on the results. Finally, γ_s^{XY} is computed for each XY case using Equation 10 and single-surface energy γ_s^i, *i.e.*, $\gamma_s^{Al_1}$, $\gamma_s^{Al_2}$ and γ_s^O, are derived using Equation 11.

$$\gamma_s^i = \gamma_s^{ij} + \gamma_s^{ik} - \gamma_s^{jk} \tag{11}$$

where i, j and k refer to the three different terminations.

Figure 3 illustrates α-Al_2O_3 basal-surface configurations before and after energy minimization. Al_1Al_2 simulations show comparable relaxed configurations (whatever the potential or charge summation method used) with both Al surface-ending layers about to merge with their O respective sublayer (Figure 3c) as already observed in Refs. [96, 97, 90, 44]. For AlO_1 and OAl_2 simulations, a significant surface reconstruction is observed in the Al-double layer surface region as shown Figure 3e,f,g while the opposite O-single layer surface is more stable during the simulation. One can notice that Vashishta and SMTB-Q potentials show similar surface reconstruction processes especially in the Al-double layer surface region where one of the first two Al layers migrates below the first O sublayer. Besides, the Gale potential shows results that depend on the charge summation method used. On one hand, the Wolf method leads to a qualitatively similar surface reorganization process than for Vashishta or SMTB-Q potentials *i.e.*, surface reconstruction only in Al-double layer surface region (Figure 3d). However, the details of the surface reconstruction mechanism are different when compared to the two aforementioned potentials (see Figure 3g compared to 3e and 3f) and moreover the O-single layer surface is more desorganized including three consecutive Al layers over it instead of only two in the Vashishta and SMTB-Q cases. Finally, the O-terminated region reconstructs when using Ewald or MSM in the same way than in the Al_1Al_2 case (see Figure 3d) *i.e.*, only a Al-single layer configuration with an energy of about 4.1 J/m^2 can be stabilized with the Gale potential when using Ewald or MSM.

Surface energies are provided in Table 6. As expected, $\gamma_s^{Al_1}$ and $\gamma_s^{Al_2}$ computed using Equation 10 are very close with differences only due to the various interatomic potentials used. Al_1O and OAl_2 simulations show particularly large energy values when compared to the more stable Al_1Al_2 configuration due to surface oxygen atoms. The values obtained using SMTB-Q for Al-terminated surface energy are in good agreement with the one of Salles *et al.* (1.89 $J.m^{-2}$) computed using the same interatomic potential [44]. This result also validates the approach we propose here. Finally, while the SMTB-Q model shows a quantitative agreement with DFT results [84, 90, 96], the

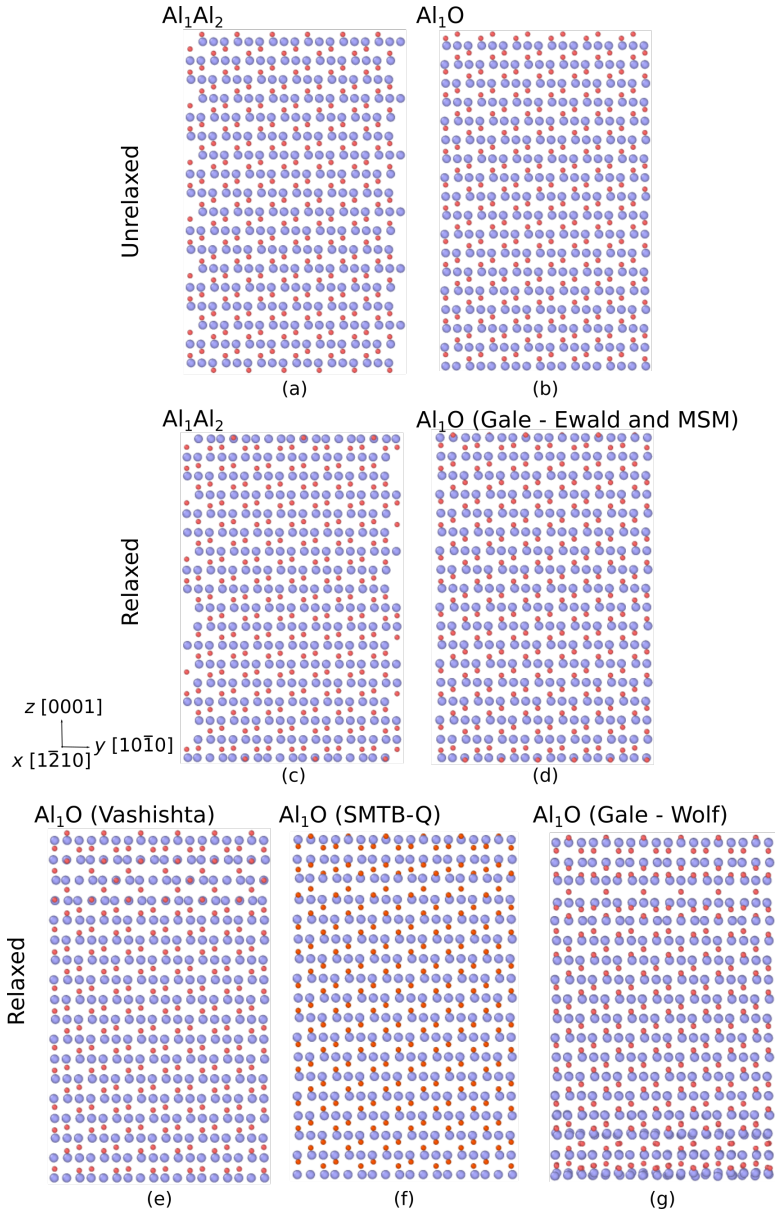

Figure 3. α-Al_2O_3 basal surface energy simulation (n_z=3). (a,b) Unrelaxed simulation cell for Al_1Al_2 and Al_1O-terminations as examples, (c) Al_1Al_2 relaxed configuration (Vashishta), (d) Al_1O relaxed configuration computed with Gale potential using the Ewald summation method (similar to MSM), (e,f,g) Al_1O relaxed configuration using respectively (e) Vashishta, (f) SMTB-Q and (g) Gale (Wolf method) interatomic potentials. Aluminum atoms are depicted in red while oxygen atoms are colored in blue.

Vashishta potential overestimates the γ_s^O while keeping γ_s^{Al} in a good range. Overall, one can conclude that the Vashishta potential is still in qualitative agreement with DFT outcomes as it confirms both $\gamma_s^O > \gamma_s^{Al}$ and the energy increase induced by O atoms in the case of Al-double layer reconstructed surfaces. The ability of the Vashishta potential to reproduce the complex Al-double layer surface reconstruction in a similar manner than the variable charge SMTB-Q potential reinforces the transferability of the potential to surface properties albeit its simple formulation. In the contrary, the Gale potential provides way larger surface energy values when compared to the other two potentials and DFT data.

Interatomic potential		**Surface energy (J.m^{-2})**		
		γ_s^O	$\gamma_s^{Al_1}$	$\gamma_s^{Al_2}$
Rigid ion	Gale	14.25	3.65	3.65
2/3-body	Vashishta	7.10	1.67	1.67
Variable charge	SMTB-Q	3.48	1.83 (1.89[44])	1.85 (1.89[44])
DFT				
Ref. [84, 90, 96]		3.98±0.48	1.92±0.21	

Table 6. (0001) surface energy in α-Al_2O_3 computed using Equation 11 and simulations using RI Gale (Wolf charge summation) [46], 2/3-body Vashishta [50] and SMTB-Q [44] interatomic potentials. Averaged DFT data calculated from Refs. [84, 90, 96] are shown for comparison.

4. Extended defects: stacking faults and dislocations

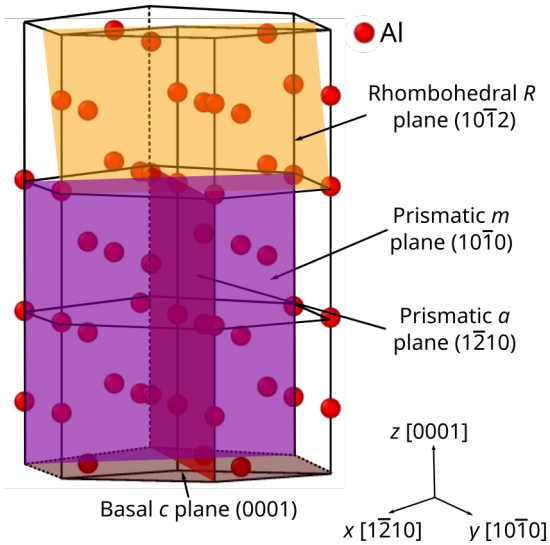

Figure 4. Main slip planes in α-Al_2O_3. Only the Al sublattice is shown for a sake of clarity.

Due to its intrinsic link with plastic deformation and mechanical properties, generalised stacking fault energy (GSFE) is one of the major lattice property to analyse when investigating the transferability of interatomic potentials to nanomechanics. The concept of stacking fault was first introduced by Vitek [98] and is now used in several atomic-scale plasticity models including dislocation or twin nucleation [99, 100], dislocation core Peierls-Nabarro modeling [101, 102] and ductile fracture modeling [103].

The basic method to compute GSFE is to build a collumnar orthogonal supercell with the longer direction normal to the faulted plane of interest. Then, atoms contained in the upper half of the supercell are shifted along an in-plane direction (forming a planar fault) and are then allowed to relax only normally to the stacking fault. Owing the perfect collumnar cell as a reference, the GSFE is defined as the energy variation normalised by the in-plane section area of the supercell. In this study, we allow supercell vectors tilting using a triclinic box to conserve 3D-PBCs along the whole simulation procedure. The simulation is performed using an iterative process including SFEs computed along either a single direction: the energy *vs.* displacement curve is thus called a γ-line, or an entire crystallographic plane leading to an energy map called γ-surface. In this study, GSFE energy minimizations are performed using a force norm criterion of 10^{-6} eV/Å when using Vashishta potential and 10^{-4} eV/Åfor SMTB-Q and Gale potentials. Results exhibit excess energies that possibly include local minima referred as stable stacking fault energy (sSFE). The sSFE relies on the stacking fault that separates dissociated dislocations as *e.g.*, $\frac{1}{6}\langle 112\rangle\{111\}$ partial dislocations in FCC metals. Thus, the calculation of the GSFE often provides guidelines to identify the possible sSF of the crystal structure and probable dislocation dissociation paths as well as quantifying their ease to appear in the crystal *i.e.*, the lower the sSFE, the easier the dislocation dissociation process. Along the years, several dislocation processes were discussed in α-Al_2O_3 including the well-known climbing dissociation of basal dislocations [33]. Twinning in the basal and rhombohedral slip plans were also observed confirming the crucial role played by stacking faults among α-Al_2O_3 plastic deformation [104, 105].

4.1. The basal (0001) stacking fault energies

A 3×2×8 supercell oriented along x=[$1\bar{2}10$], y=[$10\bar{1}0$] and z=[0001] is constructed for (0001) GSF calculations with translation vectors along x=[$1\bar{2}10$] and y=[$10\bar{1}0$] (see Figure 5). As previously discussed, (0001) planes are made of three possible atomic layers in α-Al_2O_3 referred here as O, Al_1 and Al_2. This results into two possible cutting planes *i.e.*, between an O and an Al (Al_1 or Al_2) plane or between an Al_1 and an Al_2 plane. Both configurations are investigated here using the Gale, the Vashishta and the SMTB-Q potentials. Figure 6a shows that cutting between two consecutive cationic and anionic planes lowers the SFE whatever the interatomic potential. Thus, only the lower energy basal GSFE with cutting plane between Al and O will be discussed in the following.

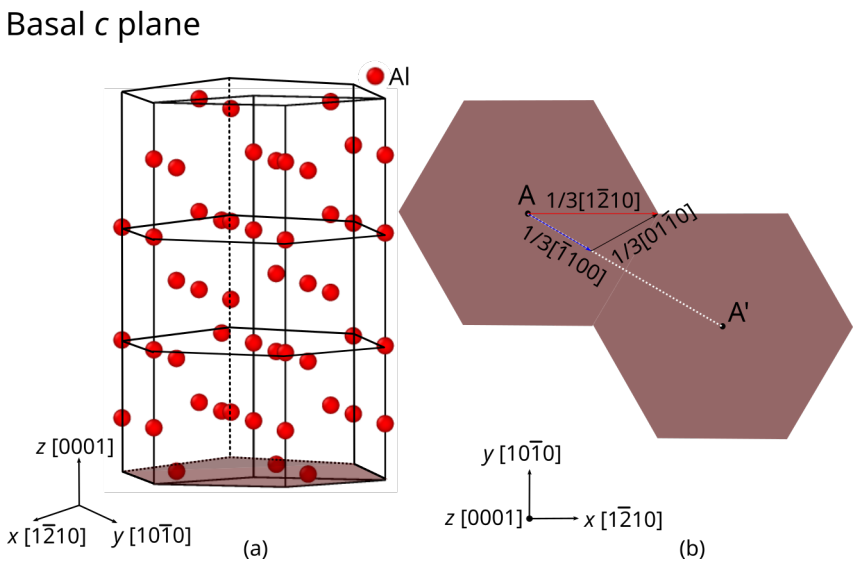

Figure 5. Illustration of the (0001) basal plane in α-Al_2O_3, (a) within the α-Al_2O_3 unit cell, red atoms refer to the Al sublattice, (b) in-plane projected view and important directions for basal stacking fault simulation.

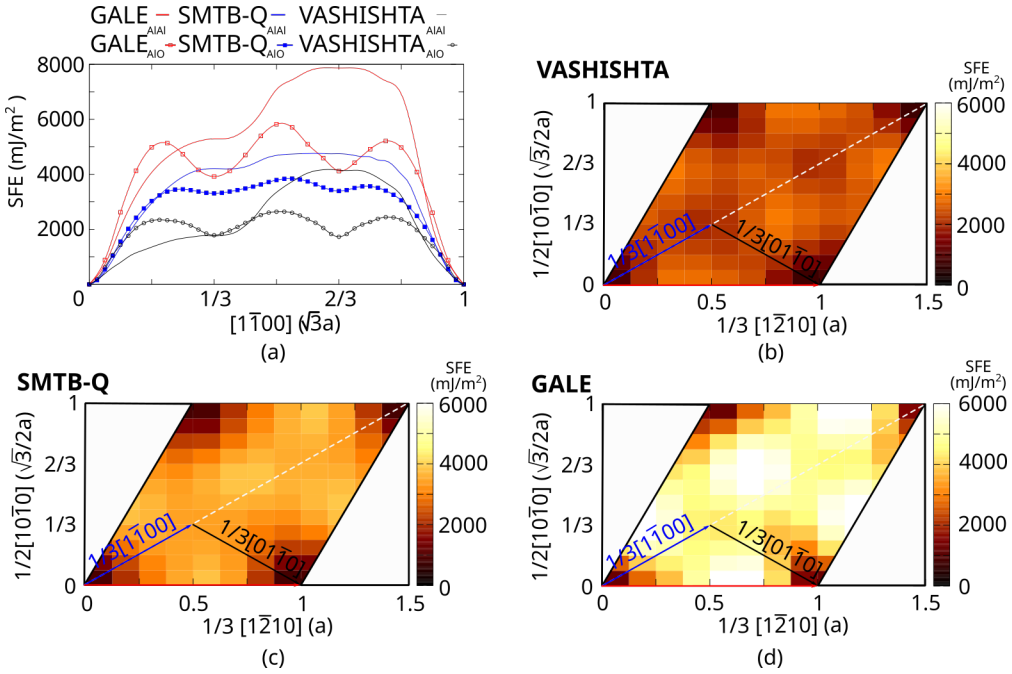

Figure 6. Stacking fault energy in the (0001) basal plane. (a) [1$\bar{1}$00] basal γ-lines with cutting planes between consecutive Al and O plans (dashed curves) and between two Al plans (plain curves). (b)-(d) Basal γ-surfaces computed using (b) Vashishta, (c) SMTB-Q and (d) Gale interatomic potentials, respectively.

The (0001) γ-surface computed with the various potentials are shown in Figure 6b to d. An energy local minimum is found for a translation vector $\overrightarrow{b_1}=\frac{1}{3}[1\bar{1}00]$ leading to a sSFE of 1785.6, 3307.7 and 3917.8 mJ.m^{-2}, respectively for the Vashishta, SMTB-Q and Gale interatomic potentials. The Vashishta potential shows the lowest sSFE when compared

to the two other potentials. This result is in good agreement with first-principles data of about 1700-1800 mJ.m^{-2} [71]. The $\frac{1}{3}[1\bar{1}00]$ sSFE is typical of the hcp structure as *e.g.*, in zirconium where the sSFE is characterized by a lower energy value of ∼200 mJ.m^{-2} due to the weaker metallic bound [106]. The shape of the basal γ-surface as computed by the three potentials is comparable *i.e.,* they show energy extrema for same translation vectors. However, overall, the Vashishta and Gale potentials show respectively lower and larger energy levels when compared to SMTB-Q. The basal γ-surface suggests a possible split of the $\overrightarrow{b}=\frac{1}{3}[1\bar{2}10]$ Burgers vector into $\overrightarrow{b_1}+\overrightarrow{b_2}=\frac{1}{3}[1\bar{1}00]+\frac{1}{3}[0\bar{1}10]$ in a similar manner than in the model proposed by Kronberg [107]. However, this dissociation has never been observed experimentally (in the basal plane) possibly due to the high-energy level of the basal sSFE. The dissociation of basal dislocations will be further discussed in the following.

4.2. The prismatic $\{10\bar{1}0\}$ *and* $\{1\bar{2}10\}$ *stacking fault energies*

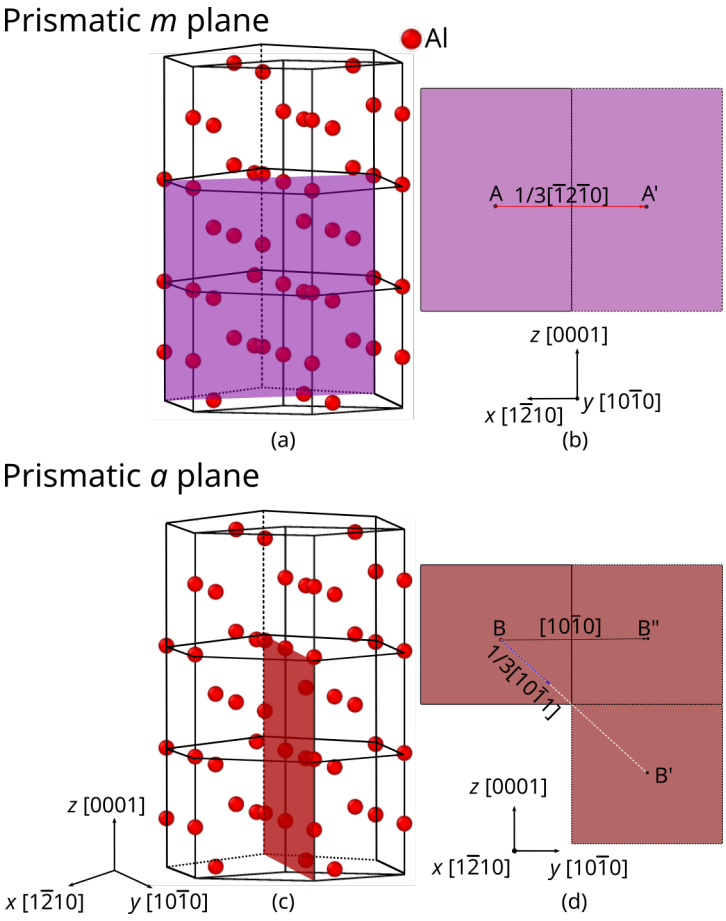

Figure 7. Representation of the prism m and a planes using perspective and in-plane projected views. (a,b) $\{10\bar{1}0\}$ prismatic m plane and (c,d) $\{1\bar{2}10\}$ prismatic a plane. Atoms colored in red rely on the Al sublattice.

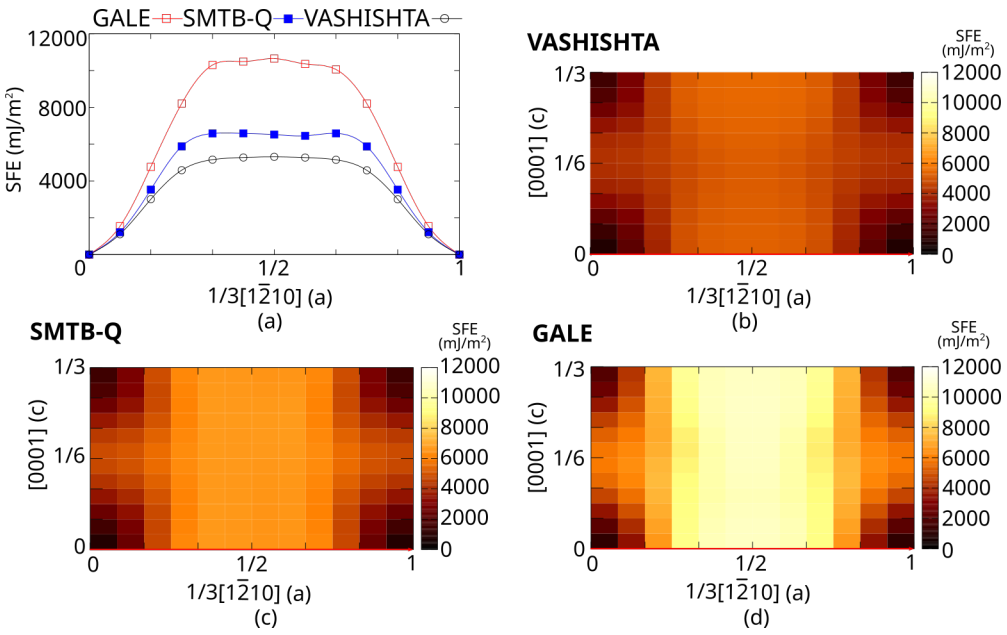

Figure 8. Stacking fault energy in the prismatic m plane $\{10\bar{1}0\}$. (a) $\frac{1}{3}[1\bar{2}10]$ γ-line, (b)-(d) Prism m γ-surfaces computed using (b) Vashishta, (c) SMTB-Q and (d) Gale interatomic potentials, respectively.

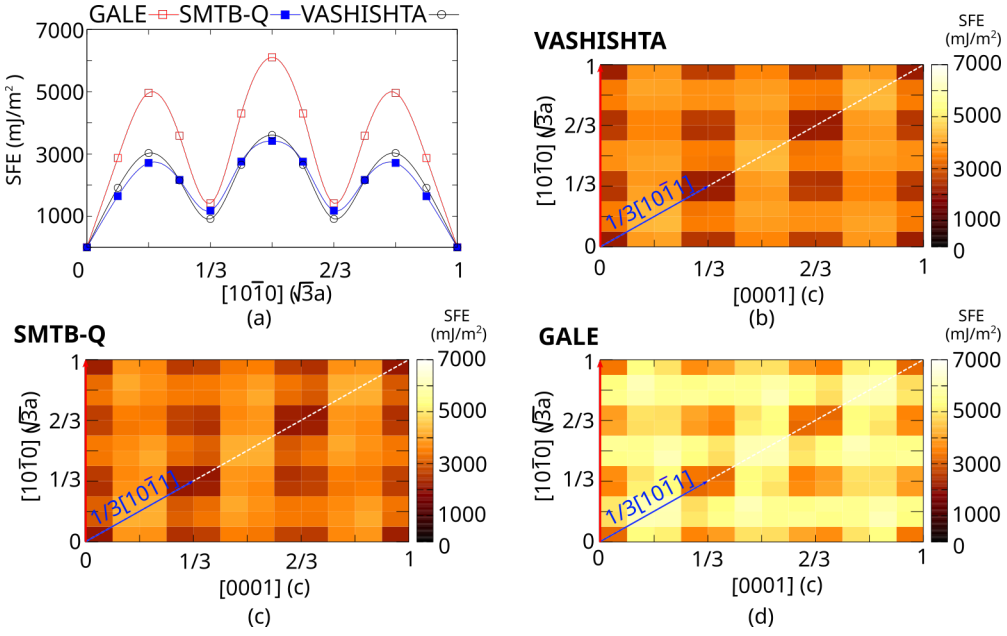

Figure 9. Stacking fault energy in the prismatic a plane $\{1\bar{2}10\}$ (a) $[10\bar{-}10]$ γ-line, (b)-(d) Prism a γ-surfaces computed using (b) Vashishta, (c) SMTB-Q and (d) Gale interatomic potentials, respectively.

Prismatic m $\{10\bar{1}0\}$ and a $\{1\bar{2}10\}$ planes are illustrated Figures 7. To compute the m plane GSF, the simulation supercell is oriented with x=$[1\bar{2}10]$ and z=[0001] (the displacement directions) while the y axis is normal to the slip plane. On the other hand, simulation cell for the a plane GSF has the x axis direction normal to the fault plane

and shift vectors along m and c directions. The m plane γ-surface and $\overrightarrow{b} = \frac{1}{3}[1\bar{2}10]$ γ-line are shown in Figure 8 for the Gale, Vashishta and SMTB-Q interatomic potentials. The results only show unstable stacking fault configurations again in a similar fashion than in the Zr case [106]. The maximum of the unstable SFE (uSFE) ranges from 5312 mJ.m^{-2} (Vashishta) up to 10650 mJ.m^{-2} (Gale) for x=$\frac{1}{6}[1\bar{2}10]$. This particularly high-energy of uSF is reproduced using the SMTB-Q potential (6584 mJ.m^{-2}). Hence, this property suggests the m plane inadequacy for slip in α-Al_2O_3 what is confirmed by the lack of experimental evidence for this slip system.

Figure 9 shows the prismatic a plane γ-surface as well as the $[10\bar{1}0]$ γ-line computed using the same three potentials. In this case, SMTB-Q and Vashishta potentials provide very close GSF values while the Gale potential show exceeding values. Three local minima are observed along the $[10\bar{1}0]$ direction. They correspond to the well-known $\frac{1}{3}[10\bar{1}0]$ dissociation path of the $\overrightarrow{b}$=$[10\bar{1}0]$ Burgers vector dislocation within the prism a plane [104, 105]. The prism a sSFE energy is about 911.5 mJ.m^{-2}, 1178.9 mJ.m^{-2} and 1411.4 mJ.m^{-2}, respectively for the Vashishta, the SMTB-Q and the Gale potentials. One can notice from the γ-surface that perfect crystal equivalent positions are also identified at $\frac{1}{3}[10\bar{1}1]$ and $\frac{2}{3}[10\bar{1}1]$, as expected from crystallography. Those equivalent positions are separated by single-hump energy barriers about twice larger than those of the $\frac{1}{3}[10\bar{1}0]$ direction. Due to its low sSFE, the prism a plane plays a key-role in α-alumina plasticity that will be discussed in the last section of the study.

4.3. The rhombohedral $\{01\bar{1}2\}$ stacking fault energies

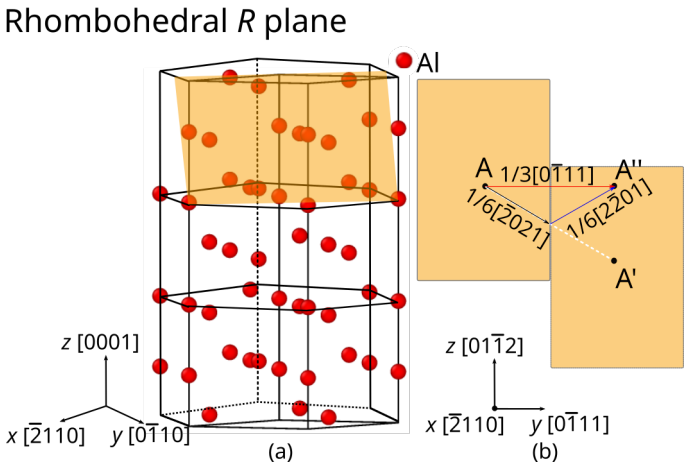

Figure 10. Illustration of a $\{01\bar{1}2\}$ rhombohedral plane, (a) within the α-Al_2O_3 unit cell, red atoms refer to the Al sublattice, (b) in-plane projected view and important directions required for the R plane stacking fault simulation.

The $\{01\bar{1}2\}$ rhombohedral (R) plane is reported as the one of the two host plane for twinning (with the c plane) in α-Al_2O_3 [108, 109, 110]. An illustration of the R plane

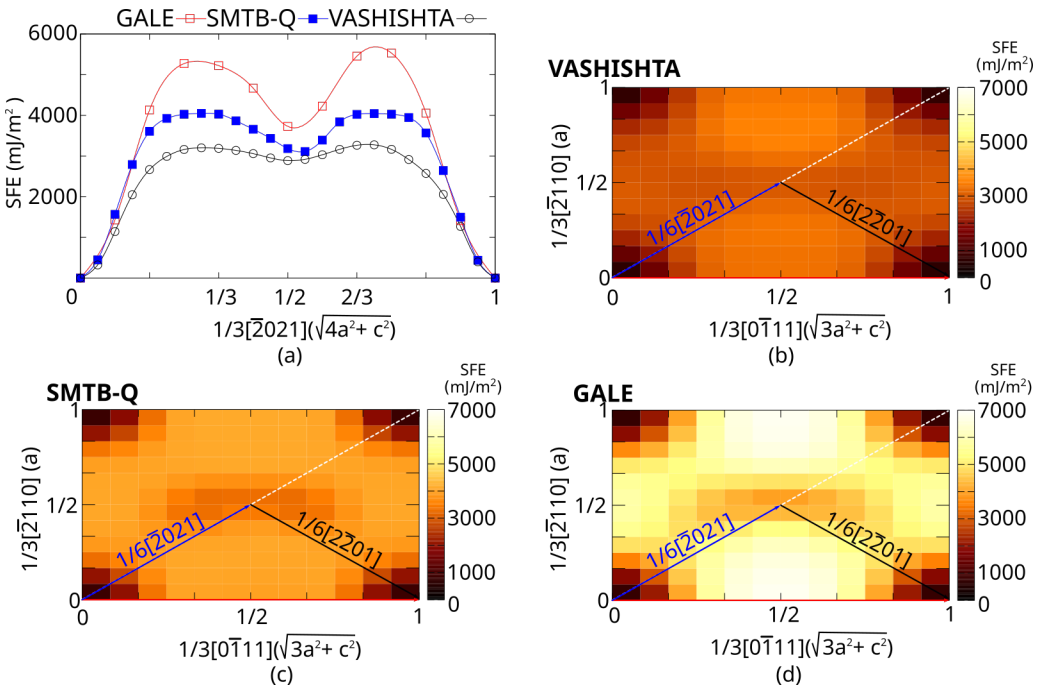

Figure 11. Rhombohedral $\{01\bar{1}2\}$ stacking fault energy. (a) $[\bar{2}021]$ γ-line, (b)-(d) γ-surfaces computed using (b) Vashishta, (c) SMTB-Q and (d) Gale interatomic potentials, respectively.

is provided Figure 10. In this study, the supercell for R plane GSF calculation is built rotating the original supercell by 58° around the $[1\bar{2}10]$ axis leading to the x=$[11\bar{2}0]$, y=$[\bar{1}101]$ and z=$[1\bar{1}02]$ orientation.

The R γ-surface computed with the various potentials is illustrated Figure 11. As for the other cases, Vashishta and SMTB-Q potentials show quantitatively comparable results that are mainly overestimated by the Gale potential. Whatever the potential, the GSF suggests a dissociation path from $\overrightarrow{b}=\frac{1}{3}[0\bar{1}11]$ into smaller $\langle\bar{2}021\rangle$-type Burgers vectors but no local minima at (or close to) $\frac{1}{21.9}[0\bar{1}11]$ as sometimes proposed in the context of rhombohedral twinning [111, 110] even using coarsen resolution simulations.

4.4. Discussion about stacking fault energy simulations

Overall, GSFE computed using the Vashishta potential are comparable to those computed using the more detailed SMTB-Q in the contrary to Gale potential outcomes that are significantly larger. This result strengthen the transferability of the Vashishta potential to shear-related properties. The Figure 12 shows γ-lines computed in the various slip planes and along appropriate Burgers vector directions and Table 8 resumes sSFE and uSFE values as compared to available DFT data. Results suggest dissociation paths with quite low sSFE for the prism a and, as a second step, for the c slip system (respectively 911.5 and 1785.6 mJ.m^{-2}). These results agree with the prism a climbing dissociation of basal dislocations observed in experiments (see *e.g.,* [33, 112]). They

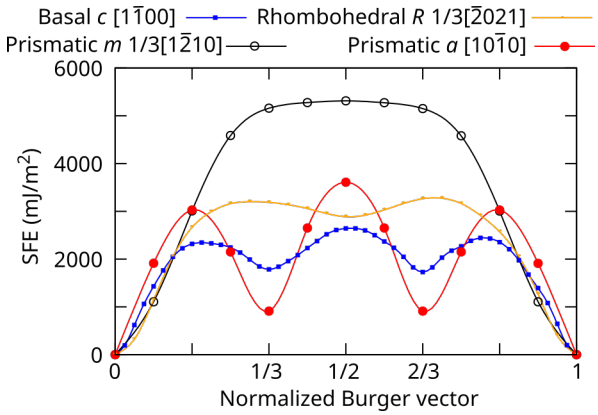

Figure 12. γ-lines computed in the c, a, m and R planes using appropriate Burgers vectors directions (see legend). Simulations are performed using the Vashishta interatomic potential.

also qualitatively justify experimental observations of basal slip and twinning [113] as well as prism a slip [31, 114]). On the other hand, only high-level GSFE extrema are noticed for the m plane γ-line (as for the entire m γ-surface) what supposes (i) no dislocation dissociation path and (ii) hard shearing capabilities, as confirmed by the lack of experimental evidences for dislocation slip in the m plane. Finally, the R plane shows a sSF configuration at $\frac{1}{6}[0\bar{2}21]$ which has a larger energy value than in the c and a cases. While elevated SFE generally decreases dissociation likelihood, one can notice that the R sSF suggested here is associated to a particularly short Burgers vector of about 3.50 Å (see Table 7) what might counteract the energy criterion. However, it is worth noticing that the sSF configuration computed in the R plane is characterized by a translation vector significantly different than the $\frac{1}{21.9}[0\bar{1}11]$ suggested in the literature [111, 110, 105]. Additional simulations using *e.g.* DFT and various R plane stacking or atom reshuffling [115] could help to conclude about this specific point.
Finally, GSFE simulations suggest a high-transferability of the Vashishta potential toward shearing properties while the discrepancies noticed when using the RI Gale potential are confirmed. In the last section, we will focus on the ability of the Vashishta potential to model the well-known basal edge dislocation. As in the entire study, results will be compared to SMTB-Q outcomes as well as to the current literature.

4.5. The basal edge dislocation

In α-alumina, the basal $\frac{1}{3}\langle 1\bar{2}10\rangle(0001)$ dislocation is known to be the most common to appear during high-temperature deformation [104, 105, 33]. Moreover, the $\frac{1}{3}\left\langle 1\bar{2}10\right\rangle$ edge dislocation can dissociate into two partial dislocations with $\frac{1}{3}\left\langle 10\bar{1}0\right\rangle$ Burgers vectors (see Equation 12). It is known that the dissociation process operates along the [0001] direction within a prismatic plane via a climbing mechanism resulting into two 60° mixed dislocations [33].

Slip plane	$\overrightarrow{b}$	$\overrightarrow{b_p}$	**Burgers vector length (Å)**
(0001)	$\frac{1}{3}\langle 11\bar{2}0\rangle$	$\frac{1}{3}\langle 1\bar{1}00\rangle$	4.72, 2.73
$\{10\bar{1}0\}$	$\frac{1}{3}\langle 11\bar{2}0\rangle$		4.72
$\{1\bar{2}10\}$	$\frac{1}{3}\langle\bar{1}101\rangle$		5.16
	$\langle 10\bar{1}0\rangle$	$\frac{1}{3}\langle 10\bar{1}0\rangle$	8.18, 2.73
$\{01\bar{1}2\}$	$\frac{1}{3}\langle 0\bar{1}11\rangle$	$\frac{1}{6}\langle\bar{2}021\rangle$	5.16, 3.50

Table 7. Slip planes and expected Burgers vectors in α-Al_2O_3. $\overrightarrow{b}$ and $\overrightarrow{b_p}$ refers to perfect and partial dislocations, respectively.

Fault plane	**Shift direction**	**SFE ($mJ.m^{-2}$)**			
		Vashishta	Gale	SMTB-Q	DFT
(0001)	$\frac{1}{6}[1\bar{1}00]$(u)	2345.1	5133.9	3455.4	
	$\frac{1}{3}[1\bar{1}00]$(s)	1785.6	3917.8	3307.7	1700-1800[71]
	$\frac{1}{2}[1\bar{1}00]$(u)	2642.7	5822.6	3791.4	
$\{10\bar{1}0\}$	$\frac{1}{6}\langle 11\bar{2}0\rangle$(u)	5312.1	10650.9	6584.2	
$\{1\bar{2}10\}$	$\frac{1}{6}\langle 10\bar{1}0\rangle$(u)	3027.9	4966.9	2711.8	2250-2800[116]
	$\frac{1}{3}\langle 10\bar{1}0\rangle$(s)	911.5	1411.4	1178.9	350-720[117, 116]
	$\frac{1}{2}\langle 10\bar{1}0\rangle$(u)	3608.9	6107.0	3419.8	
$\{01\bar{1}2\}$	$\frac{1}{12}\langle\bar{2}021\rangle$(u)	3200.8	5374.0	4047.6	
	$\frac{1}{6}\langle\bar{2}021\rangle$(s)	2886.7	3726.9	3110.0	

Table 8. SFE computed in the various slip planes of α-Al_2O_3 using the Gale [46], 2/3-body Vashishta [50] and the many-body SMTB-Q [44] interatomic potentials as compared to DFT data avaiblable in the litterature.

$$\frac{1}{3}[11\bar{2}0] \rightarrow \frac{1}{3}[10\bar{1}0] + \frac{1}{3}[01\bar{1}0] \tag{12}$$

Still, a net controversy persists about the partial dislocation core structures for which two models are discussed in the literature. On one hand, Kronberg *et al.* proposed that slip occurs between two consecutive Al and O layers [107]. This slip model involves charge transport due to the ionic bonding between Al and O atoms. On the other hand, Bilde-Sørensen *et al.* proposed a mixed partial core that glides between two consecutive puckered Al layers without charge transfer [32]. The various dislocation core models are illustrated Figure 13. While Shibata *et al.* [118] confirmed Kronberg's core hypothesis using high-resolution scanning transmission electron microscopy, Heuer *et al.* [33] produced a markedly detailed atomic model of the dislocation cores with Al-Al terminated partial dislocations using the negative spherical-aberration imaging technique supporting the Bilde-Sørensen's model.

In the following, we extent the original work of Tsuruta *et al.* [112] by investigating

both Al/O-terminated or Al/Al-terminated basal partial dislocations using both the 2/3-body Vashishta and the variable charge SMTB-Q potentials.

4.5.1. Methodology

As shown Figure 13, a dipole of edge basal dislocations is introduced in a 73.13×0.83×144.97 nm^3 simulation cell following the approach proposed by Tsuruta *et al.* to allow a direct comparison of simulation outcomes. In their original study, the authors chose this size large enough to avoid size-effect. Each $\frac{1}{3}\langle 11\bar{2}0\rangle$ dislocation is introduced as a pair of mixed partial dislocation separated by 2 nm long stacking faults within the prismatic plane. This length corresponds to the lowest energy configuration computed by Tsuruta *et al.* using the same Vashishta potential. The partial dislocation pairs are either Al/Al- (Figure 13(b,d)) or Al/O-terminated (Figure 13(c,e)) as in the two models of Bilde-Sørensen and Kronberg respectively. After removing corresponding Al and O atoms on planes perpendicular to the basal plane, the empty region is closed applying the linear elastic theory [119].

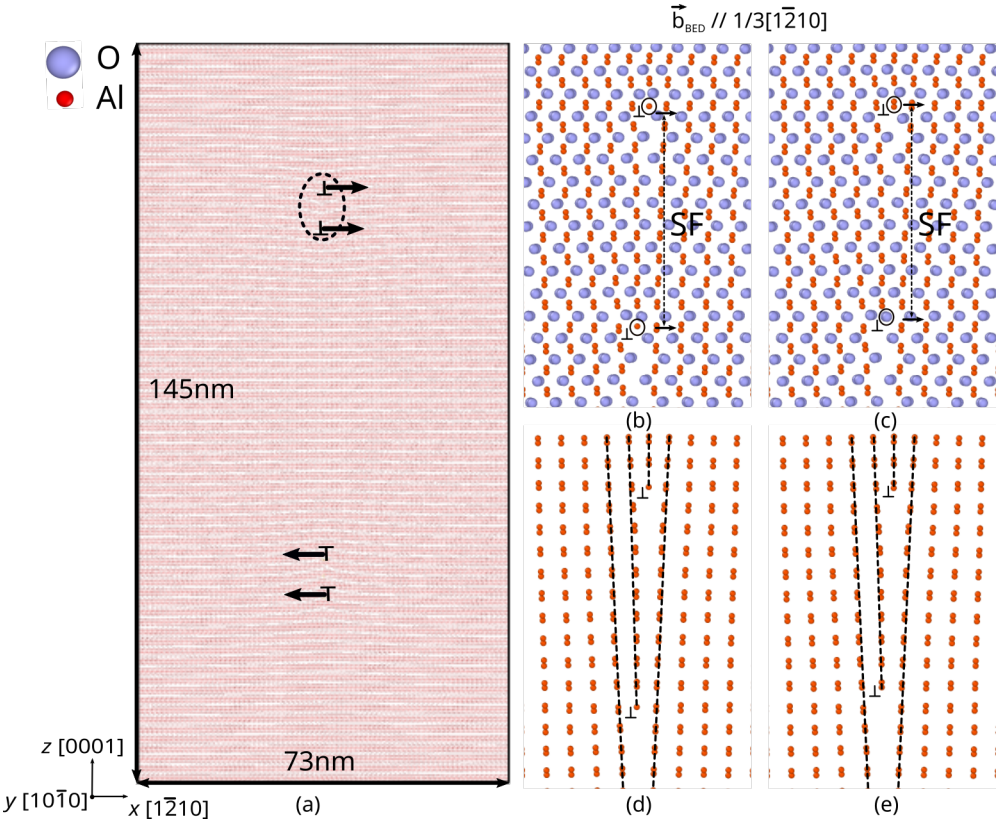

Figure 13. Unrelaxed basal edge dislocation core structure. (a) Simulation cell and edge dislocation dipole. (b) Al/Al-terminated dislocation core (Bilde-Sørensen's model), (c) Al/O-terminated dislocation core (Kronberg's model), (d) and (e) illustrate respective cation sublattices.

After construction, the system is then relaxed using the Vashishta potential and a procedure close to the one of Tsuruta. First, the energy is minimized using the FIRE algorithm and a force norm criterion of 10^{-6} eV/Å (minimized #1 configuration). Then, a low-temperature shake is performed during 50 ps using the NPT ensemble (anisotropic pressure relaxation) and the Nosé-Hoover thermostat (timestep dt=1 ps) in order to remove residual stresses, as in the work of Tsuruta. Then, the system is further relaxed using a combination of conjugate gradient and FIRE minimization runs with the same force norm criterion of 10^{-6} eV/Å (minimized #2 configuration). Secondly, the Vashishta final configuration is used as an input for SMTB-Q potential calculations: the potential energy is first minimized using the FIRE algorithm and a quite large force norm target. At this stage (SMTB-Q minimized #1 configuration), a residual hydrostatic pressure of few GPa due to the lattice parameter deviation between the two interatomic potentials is noticed. Then, a pressure relaxation simulation (performed at T=0K) and a final minimization run are consecutively performed down to a net force norm of 10^{-2} eV/Å (minimized #2 configuration).

4.5.2. Results and discussion

Figure 14 shows partially and fully relaxed configurations for Kronberg (Al/O-terminated) and Bilde-Sørensen (Al/Al-terminated) dislocation models using both the Vashishta and SMTB-Q interatomic potentials. *Minimization #1* refers to the outcome of the first minimization episode (whatever the interatomic model used) while *Minimization #2* refers to (i) the minimization outcome after the NPT run in the case of the Vashishta potential and (ii) the minimization outcome after the box relaxation run in SMTB-Q case. Due to the perfect symmetry observed, only one dislocation extracted from the original dislocation dipole is shown and discussed in the following.

Dislocation core configurations obtained using the Vashishta potential are similar to those of Tsuruta *et al.* using the same interatomic potential. The two mixed partial dislocation exhibit particularly different structures whatever the Al/Al- or Al/O-terminated configuration. When compared to the unrelaxed structure shown Figure 13, the fully-relaxed top cores (single-Al or double-Al terminated respectively for Bilde-Sørensen and Kronberg models) shown Figure 14c,g are characterized by a regular dislocation core relaxation process that adapts the local mismatch while the bottom cores (either single-Al or single-O terminated respectively for Kronberg or Bilde-Sørensen model) are characterized by an extended fault in the Al puckered layer. As in the work of Tsuruta *et al.*, we also noticed the larger extent of the Al fault for the Al/Al-terminated dislocation model when using the Vashishta interatomic potential.

Topological configurations obtained using the variable charge potential SMTB-Q are particularly similar to those obtained using the Vashishta potential. This feature is quantified here using the displacement vector analysis after *Minimization #1* shown in Figure 14b,f taking respective inputs as reference file. Indeed, the maximum displacement computed between the fully-relaxed Vashishta configuration and the partially-

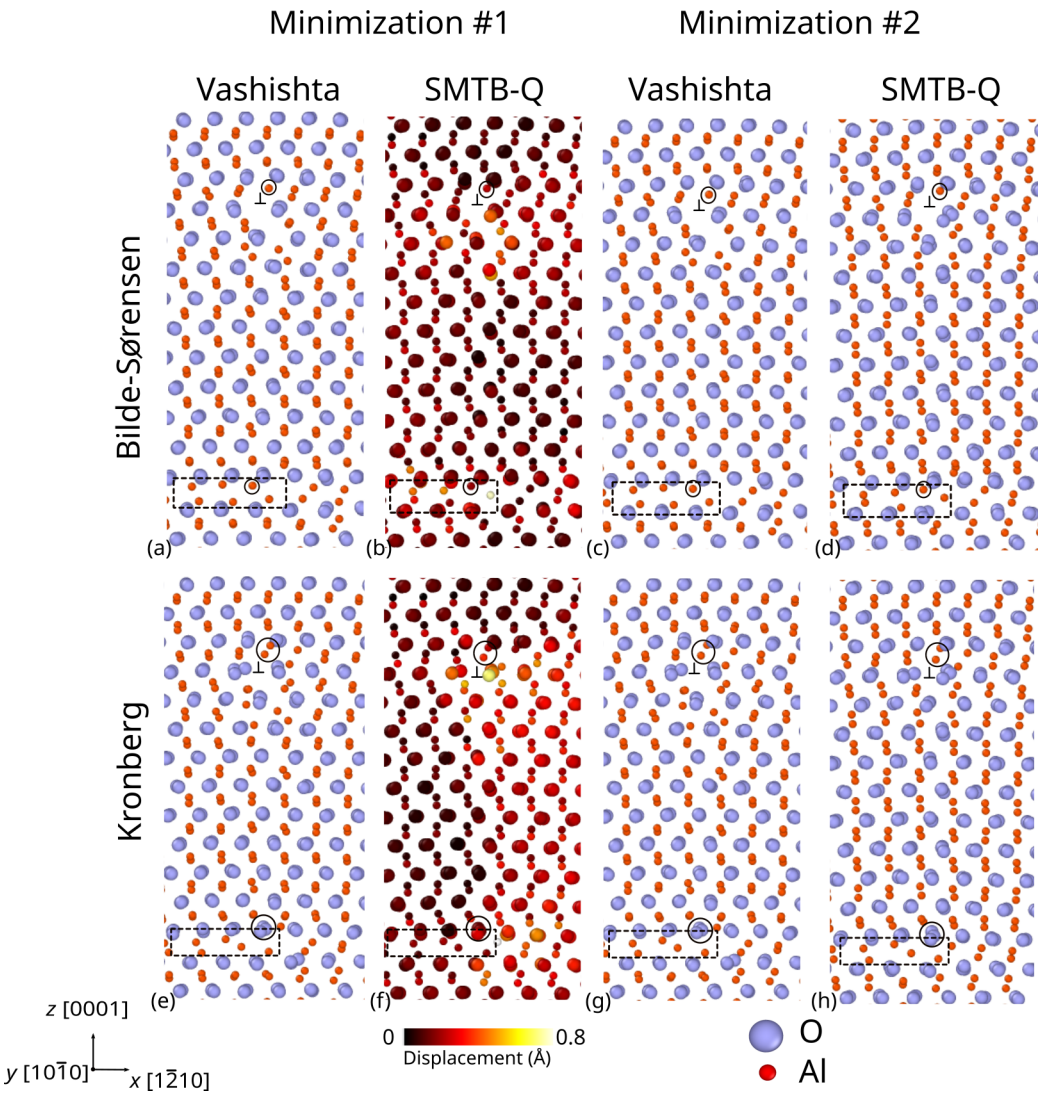

Figure 14. Dislocation core for (a:d) Al/Al-terminated (Bilde-Sørensen) and (e:h) Al/O-terminated (Kronberg) dislocations computed using the Vashishta and SMTB-Q interatomic potentials. Minimization #1 refers to the initial minimization run result while Minimization #2 refers to (i) the minimized configuration after NPT relaxation for Vashishta and (ii) the minimized configuration after box relaxation in the SMTB-Q case. Atoms surrounded by black circles refer to dislocation-termination atoms. The dashed rectangle emphasizes the puckered Al layers in which the bottom dislocation fault extends. (b,f): atoms are colored according to the displacement vector amplitude calculation. For each case, the reference structure is the input configuration *i.e.*, the fully-relaxed Vashishta configuration presented in c) and g) respectively.

relaxed SMTB-Q configuration (before simulation box relaxation) located deep in the dislocation core is lower than 1 Å what confirms the similarity between the two configurations as well as the weak effect of the residual pressure terms (few GPa) on the core structure. One can note that the SMTB-Q *Minimization #1* core configuration is characterized by relative atomic displacements of the same order of magnitude in the three directions of space. Here again using the SMTB-Q potential, the top core is characterized by a regular core relaxation without particular directional extension while the bottom core show an extended planar fault within the Al puckered layer. However, one can notice two particular changes specific to the SMTB-Q potential (i) the oxygen atoms in the top core are slightly more disorganized and (ii) the bottom core planar fault is less extended for both models, when compared to the Vashishta potential. Nevertheless, these differences remain quite acceptable having in mind the simplicity of the 2/3-body Vashishta potential when compared to the more complex SMTB-Q.

A simplified calculation of the dislocation energy E_{dislo} can be derived using the simulation cell energy with and without defect:

$$E_{dislo} = \frac{E_{tot} - n.E_{coh}}{2L} \tag{13}$$

where E_{tot} is the minimized energy of the simulation as computed after *Minimization #2*, n is the number of atoms, E_{coh} is the per-atom cohesive energy and L is the dislocation length.

Equation 13 can be used to qualitatively compare interatomic potential tendencies as presented in Table 9. Results confirm prior topological observations with only slight energy variations between Kronberg and Bilde-Sørensen models. Here, the comparison between Vashishta and SMTB-Q leads to (i) similar topological configurations, (ii) comparable range of energy and, the most important, (iii) similar relative energy trends *i.e.*, E_{dislo} is slightly lower in the Bilde-Sørensen case than in the Kronberg one. Having in mind the previous outcomes on GSFE, this results appears as an additional confirmation of the Vashishta potential transferability to nanomechanics.

5. Conclusion

α-alumina is a widely used ceramic that benefits of a renewed interest at the nanoscale in order to better assess the elementary mechanisms that govern ceramic fabrication processes such as compaction and sintering. The aim of this study was to evaluate the transferatiblity of a bench of various interatomic potentials towards small-scale nanomechanics applications. Lattice parameters, elastic constants, surface and stacking-fault energies as well as dislocation properties were investigated using rigid ion, 2/3-body and many-body variable charge potentials leading to the following conclusions:

	Vashishta		**SMTB-Q**	
E_{coh} (eV/at.)	-6.35		-6.40	
	Al/Al	**Al/O**	**Al/Al**	**Al/O**
n	1019720	1019700	1019720	1019700
E_{tot} (eV)	-6475206.6	-6475074.6	-6528738.4	-6528609.4
L (Å)	8.18		8.32	
E_{dislo} (eV/Å)	14.44	14.74	18.59	18.65

Table 9. Dislocation energy as computed using Equation 13 respectively for Kronberg Al/O and Bilde-Sørensen Al/Al dislocation model using the Vashishta and the SMTB-Q potentials.

- Most of the potentials tested succeed in computing lattice parameters of α-Al_2O_3 but RI potentials generally show large discrepancies when computing elastic constants (all except the Gale parameterization [46]). However, these latter are correctly reproduced by the 2/3-body Vashishta and the SMTB-Q potentials.
- The 2/3-body Vashishta and variable charge SMTB-Q potentials provide similar topological outcomes and energy values for the various (0001) surface terminations. Same conclusions are drawn for stacking fault energy calculations in several slip plans of the crystalline structure. These results are in good agreement with already published DFT data and experiments while the Gale rigid ion potential overestimates surface and stacking fault energies and show different topological configurations.
- The basal edge dislocation structure as computed using the Vashishta potential compare successfullly to the more sophisticated SMTB-Q. Furthermore, both potentials show similar dislocation energy trends that confirm a slighlty lower core energy for the basal edge dislocation derived from the Bilde-Sørensen model.

Finally, among the interatomic potentials investigated here, the Vashishta and the SMTB-Q potentials appear as the more suited to compute α-Al_2O_3 material properties relevant for nanomechanical applications. While the RI parameterizations rapidly fail at reproducing surface and stacking fault energies, the 2/3-body Vashishta potential has demonstrated to be the best alternative to the more costly variable charge potentials with only slight discrepancies when compared to DFT and the experimental literature data. Finally, this study confirms the transferability of the 2/3-body Vashishta interatomic potential that could easily and carefree be used in the future for large-scale atomistic applications in the field of nanomechanics.

Acknowledgements

The authors are grateful to the Fédération Lyonnaise de Modélisation et Sciences Numériques (FLMSN) partner of the EQUIPEX EQUIP@MESO that provides the HPC

resources as well as to Pr. P. Lagerlöf for the meaningfull discussions.

Conflict of interest

The authors confirm no conflict of interest.

References

[1] You Wang, Stephen Jiang, Meidong Wang, Shihe Wang, T Danny Xiao, and Peter R Strutt. Abrasive wear characteristics of plasma sprayed nanostructured alumina/titania coatings. *Wear*, 237(2):176–185, 2000.

[2] Xie Nie, EI Meletis, JC Jiang, A Leyland, AL Yerokhin, and A Matthews. Abrasive wear/corrosion properties and TEM analysis of Al_2O_3 coatings fabricated using plasma electrolysis. *Surface and Coatings Technology*, 149(2-3):245–251, 2002.

[3] H Knözinger and Ph Ratnasamy. Catalytic aluminas: surface models and characterization of surface sites. *Catalysis Reviews Science and Engineering*, 17(1):31–70, 1978.

[4] Akkarat Manasilp and Erdogan Gulari. Selective CO oxidation over Pt/alumina catalysts for fuel cell applications. *Applied Catalysis B: Environmental*, 37(1):17–25, 2002.

[5] Thomas J Webster, Celaletdin Ergun, Robert H Doremus, Richard W Siegel, and Rena Bizios. Enhanced functions of osteoblasts on nanophase ceramics. *Biomaterials*, 21(17):1803–1810, 2000.

[6] Jerome Chevalier and Laurent Gremillard. Ceramics for medical applications: A picture for the next 20 years. *Journal of the European Ceramic Society*, 29(7):1245–1255, 2009.

[7] P Boutin. L'arthroplastie totale de la hanche par prothèse en alumine. *International Orthopaedics*, 1(2):87–94, 1977.

[8] SF Hulbert. The use of alumina and zirconia in surgical implants. *Advanced Series in Ceramics*, 1:25–40, 1993.

[9] JE Nevelos, F Prudhommeaux, M Hamadouche, C Doyle, E Ingham, A Meunier, AB Nevelos, L Sedel, and J Fisher. Comparative analysis of two different types of alumina-alumina hip prosthesis retrieved for aseptic loosening. *The Journal of Bone and Joint Surgery. British Volume*, 83(4):598–603, 2001.

[10] Isabelle Denry and Julie A Holloway. Ceramics for dental applications: a review. *Materials*, 3(1):351–368, 2010.

[11] Fadhel A Al-Sanabani, Ahmed A Madfa, and Nasr H Al-Qudaimi. Alumina ceramic for dental applications: A review article. *American Journal of Materials Research*, 1(1):26–34, 2014.

[12] David J Green. Critical microstructures for microcracking in Al_2O3-ZrO_2 composites. *Journal of the American Ceramic Society*, 65(12):610–614, 1982.

[13] WH Tuan, RZ Chen, TC Wang, CH Cheng, and PS Kuo. Mechanical properties of Al_2O_3/ZrO_2 composites. *Journal of the European Ceramic Society*, 22(16):2827–2833, 2002.

[14] Ramazan Yilmaz, Ali Osman Kurt, Adem Demir, and Zafer Tatli. Effects of TiO_2 on the mechanical properties of the Al_2O_3–TiO_2 plasma sprayed coating. *Journal of the European Ceramic Society*, 27(2-3):1319–1323, 2007.

[15] Long He, Yefa Tan, Xiaolong Wang, Ting Xu, and Xiang Hong. Microstructure and wear properties of Al_2O_3-CeO_2/Ni-base alloy composite coatings on aluminum alloys by plasma spray. *Applied Surface Science*, 314:760–767, 2014.

[16] Vikas Verma and BV Manoj Kumar. Synthesis, microstructure and mechanical properties of $Al_2O_3/ZrO_2/CeO_2$ composites with addition of nickel and titania processed by conventional sintering. *Materials Today: Proceedings*, 4(2):3062–3071, 2017.

[17] E Mohammad Sharifi, F Karimzadeh, and MH Enayati. A study on mechanochemical behavior of B_2O_3-Al system to produce alumina-based nanocomposite. *Journal of Alloys and Compounds*, 482(1-2):110–113, 2009.

[18] Emilie Calvié, Lucile Joly-Pottuz, Claude Esnouf, Philippe Clément, Vincent Garnier, Jérôme Chevalier, Yves Jorand, Annie Malchère, Thierry Epicier, and Karine Masenelli-Varlot. Real time TEM observation of alumina ceramic nano-particles during compression. *Journal of the European Ceramic Society*, 32(10):2067–2071, 2012.

[19] Emilie Calvié, Julien Réthoré, Lucile Joly-Pottuz, Sylvain Meille, Jérome Chevalier, Vincent Garnier, Yves Jorand, Claude Esnouf, Thierry Epicier, JB Quirk, et al. Mechanical behavior law of ceramic nanoparticles from transmission electron microscopy *in situ* nano-compression tests. *Materials Letters*, 119:107–110, 2014.

[20] S Korte and WJ Clegg. Discussion of the dependence of the effect of size on the yield stress in hard materials studied by microcompression of MgO. *Philosophical Magazine*, 91(7-9):1150–1162, 2011.

[21] S Korte, Martin Ritter, Chengge Jiao, PA Midgley, and WJ Clegg. Three-dimensional electron backscattered diffraction analysis of deformation in MgO micropillars. *Acta Materialia*, 59(19):7241–7254, 2011.

[22] Zehui Du, Xiao Mei Zeng, Qing Liu, Alan Lai, Shahrouz Amini, Ali Miserez, Christopher A Schuh, and Chee Lip Gan. Size effects and shape memory properties in ZrO_2 ceramic micro-and nano-pillars. *Scripta Materialia*, 101:40–43, 2015.

[23] Inas Issa, Jonathan Amodeo, Julien Réthoré, Lucile Joly-Pottuz, Claude Esnouf, Julien Morthomas, Michel Perez, Jérome Chevalier, and Karine Masenelli-Varlot. In situ investigation of MgO nanocube deformation at room temperature. *Acta Materialia*, 86:295–304, 2015.

[24] Jonathan Amodeo, Sébastien Merkel, Christophe Tromas, Philippe Carrez, Sandra Korte-Kerzel, Patrick Cordier, and Jérôme Chevalier. Dislocations and plastic deformation in MgO crystals: a review. *Crystals*, 8(6):240, 2018.

[25] Inas Issa, Lucile Joly-Pottuz, Jonathan Amodeo, David J Dunstan, Claude Esnouf, Julien Réthoré, Vincent Garnier, Jérôme Chevalier, and Karine Masenelli-Varlot. From dislocation nucleation to dislocation multiplication in ceramic nanoparticle. *Materials Research Letters*, 9(6):278–283, 2021.

[26] Dan Mordehai, Omer David, and Roman Kositski. Nucleation-controlled plasticity of metallic nanowires and nanoparticles. *Advanced Materials*, 30(41):1706710, 2018.

[27] Jonathan Amodeo and Laurent Pizzagalli. Modeling the mechanical properties of nanoparticles: a review. *Comptes Rendus. Physique*, 22(S3):1–32, 2021.

[28] Pylin Sarobol, Michael Chandross, Jay D Carroll, William M Mook, Daniel C Bufford, Brad L Boyce, Khalid Hattar, Paul G Kotula, and Aaron C Hall. Room temperature deformation mechanisms of alumina particles observed from *in situ* micro-compression and atomistic simulations. *Journal of Thermal Spray Technology*, 25(1-2):82–93, 2016.

[29] Cheng Zhang, Rajiv K Kalia, Aiichiro Nakano, Priya Vashishta, and Paulo S Branicio. Deformation mechanisms and damage in α-alumina under hypervelocity impact loading. *Journal of Applied Physics*, 103(8):083508, 2008.

[30] Kenji Nishimura, Rajiv K Kalia, Aiichiro Nakano, and Priya Vashishta. Nanoindentation hardness anisotropy of alumina crystal: A molecular dynamics study. *Applied Physics Letters*, 92(16):161904, 2008.

[31] J Castaing, J Cadoz, and SH Kirby. Deformation of Al_2O_3 single crystals between 25°C and 1800°C: basal and prismatic slip. *Le Journal de Physique Colloques*, 42(C3):C3–43, 1981.

[32] JB Bilde-Sørensen, BF Lawlor, T Geipel, P Pirouz, AH Heuer, KPD Lagerlöf, et al. On basal slip and basal twinning in sapphire (α-Al_2O_3)—i. basal slip revisited. *Acta Materialia*, 44(5):2145–2152, 1996.

[33] AH Heuer, CL Jia, and KPD Lagerlöf. The core structure of basal dislocations in deformed sapphire (α-Al_2O_3). *Science*, 330(6008):1227–1231, 2010.

[34] GV Lewis and CRA Catlow. Potential models for ionic oxides. *Journal of Physics C: Solid State Physics*, 18(6):1149, 1985.

[35] P Vashishta, Rajiv K Kalia, José P Rino, and Ingvar Ebbsjö. Interaction potential for SiO_2: A molecular-dynamics study of structural correlations. *Physical Review B*, 41(17):12197, 1990.

[36] Priya Vashishta, Rajiv K Kalia, Aiichiro Nakano, and José Pedro Rino. Interaction potential for silicon carbide: A molecular dynamics study of elastic constants and vibrational density of states for crystalline and amorphous silicon carbide. *Journal of Applied Physics*, 101(10):103515, 2007.

[37] Paulo Sergio Branicio, José Pedro Rino, Chee Kwan Gan, and Hélio Tsuzuki. Interaction potential for indium phosphide: a molecular dynamics and first-principles study of the elastic constants, generalized stacking fault and surface energies. *Journal of Physics: Condensed Matter*, 21(9):095002, 2009.

[38] Frank H Stillinger and Thomas A Weber. Computer simulation of local order in condensed phases of silicon. *Physical Review B*, 31(8):5262, 1985.

[39] RLC Vink, GT Barkema, WF Van der Weg, and Normand Mousseau. Fitting the stillinger–weber potential to amorphous silicon. *Journal of Non-crystalline Solids*, 282(2-3):248–255, 2001.

[40] Adri CT Van Duin, Siddharth Dasgupta, Francois Lorant, and William A Goddard. Reaxff: a reactive force field for hydrocarbons. *The Journal of Physical Chemistry A*, 105(41):9396–9409, 2001.

[41] Tzu-Ray Shan, Bryce D Devine, Travis W Kemper, Susan B Sinnott, Simon R Phillpot, et al. Charge-optimized many-body potential for the hafnium/hafnium oxide system. *Physical Review B*, 81(12):125328, 2010.

[42] Tao Liang, Yu-Ting Cheng, Xiaowa Nie, Wenjia Luo, Aravind Asthagiri, Michael J Janik, Evan Andrews, John Flake, and Susan B Sinnott. Molecular dynamics simulations of CO_2 reduction on Cu (111) and Cu/ZnO $(10\bar{1}0)$ using charge optimized many body potentials. *Catalysis Communications*, 52:84–87, 2014.

[43] R Tétot, A Hallil, J Creuze, and I Braems. Tight-binding variable-charge model for insulating oxides: Application to TiO_2 and ZrO_2 polymorphs. *EPL (Europhysics Letters)*, 83(4):40001, 2008.

[44] N Salles, O Politano, E Amzallag, and R Tétot. Molecular dynamics study of high-pressure alumina polymorphs with a tight-binding variable-charge model. *Computational Materials Science*, 111:181–189, 2016.

[45] Steve Plimpton. Fast parallel algorithms for short-range molecular dynamics. *Journal of Computational Physics*, 117(1):1–19, 1995.

[46] JD Gale, CRA Catlow, and WC Mackrodt. Periodic *ab initio* determination of interatomic potentials for alumina. *Modelling and Simulation in Materials Science and Engineering*, 1(1):73, 1992.

[47] T Bush, J Gale, C Catlow, and P Battle. Self-consitent interatomic potentials for the simulation of binary and ternary oxides. *Journal of Materials Chemistry*, 4(11), 1994.

[48] Jizhong Sun, T Stirner, WE Hagston, A Leyland, and A Matthews. A simple transferable interatomic potential model for binary oxides applied to bulk α-Al_2O_3 and the (0001) α-Al_2O_3 surface. *Journal of Crystal Growth*, 290(1):235–240, 2006.

[49] Slawomir Blonski and Stephen H Garofalini. Molecular dynamics study of silica-alumina interfaces. *The Journal of Physical Chemistry*, 100(6):2201–2205, 1996.

[50] Priya Vashishta, Rajiv K Kalia, Aiichiro Nakano, and José Pedro Rino. Interaction

potentials for alumina and molecular dynamics simulations of amorphous and liquid alumina. *Journal of Applied Physics*, 103(8):083504, 2008.

[51] Richard A Buckingham. The classical equation of state of gaseous helium, neon and argon. *Proceedings of the Royal Society of London. Series A. Mathematical and Physical Sciences*, 168(933):264–283, 1938.

[52] Paul P Ewald. Die berechnung optischer und elektrostatischer gitterpotentiale. *Annalen der Physik*, 369(3):253–287, 1921.

[53] D Wolf, P Keblinski, SR Phillpot, and J Eggebrecht. Exact method for the simulation of coulombic systems by spherically truncated, pairwise r^{-1} summation. *The Journal of Chemical Physics*, 110(17):8254–8282, 1999.

[54] David J Hardy, John E Stone, and Klaus Schulten. Multilevel summation of electrostatic potentials using graphics processing units. *Parallel Computing*, 35(3):164–177, 2009.

[55] Charles Richard Arthur Catlow. Point defect and electronic properties of uranium dioxide. *Proceedings of the Royal Society of London. A. Mathematical and Physical Sciences*, 353(1675):533–561, 1977.

[56] Julian D Gale. Gulp: A computer program for the symmetry-adapted simulation of solids. *Journal of the Chemical Society, Faraday Transactions*, 93(4):629–637, 1997.

[57] Masanori Matsui. Molecular dynamics study of the structures and bulk moduli of crystals in the system CaO-MgO-Al_2O_3-SiO_2. *Physics and Chemistry of Minerals*, 23(6):345–353, 1996.

[58] G Sattonnay and R Tétot. Bulk, surface and point defect properties in UO_2 from a tight-binding variable-charge model. *Journal of Physics: Condensed Matter*, 25(12):125403, 2013.

[59] R Tétot, N Salles, S Landron, and E Amzallag. $SrTiO_3$ (001) surface and strained thin films: Atomic simulations using a tight-binding variable-charge model. *Surface Science*, 616:19–28, 2013.

[60] Anthony K Rappe and William A Goddard III. Charge equilibration for molecular dynamics simulations. *The Journal of Physical Chemistry*, 95(8):3358–3363, 1991.

[61] Jacek Goniakowski and Claudine Noguera. Electronic structure of clean insulating oxide surfaces I. A numerical approach. *Surface Science*, 319(1-2):68–80, 1994.

[62] Emile Maras, Nicolas Salles, Robert Tétot, Tapio Ala-Nissila, and Hannes Jónsson. Improved tight-binding charge transfer model and calculations of energetics of a step on the rutile TiO_2 (110) surface. *The Journal of Physical Chemistry C*, 119(19):10391–10399, 2015.

[63] Aurélien Soulié, Jean-Paul Crocombette, Antoine Kraych, Frédérico Garrido, Gaël Sattonnay, and Emmanuel Clouet. Atomistically-informed thermal glide model for edge dislocations in uranium dioxide. *Acta Materialia*, 150:248–261, 2018.

[64] Aurélien Soulié, Gianguido Baldinozzi, Frédérico Garrido, and Jean-Paul Crocombette. Clusters of oxygen interstitials in UO_{2+x} and α-U_4O_9: Structure and arrangements. *Inorganic Chemistry*, 58(19):12678–12688, 2019.

[65] D Mbongo, R Tétot, R Ducher, R Dubourg, and N Salles. Improved SMTB-Q model applied to oxygen migration and pressure phase transitions in UO_2. *Journal of Physics: Condensed Matter*, 32(9):095701, 2019.

[66] Shawn P Coleman and Douglas E Spearot. Atomistic simulation and virtual diffraction characterization of stable and metastable alumina surfaces. *Acta Materialia*, 78:354–368, 2014.

[67] Shawn P Coleman and Douglas E Spearot. Atomistic simulation and virtual diffraction characterization of homophase and heterophase alumina interfaces. *Acta Materialia*, 82:403–413, 2015.

[68] JD Snow and AH Heuer. Slip systems in Al_2O_3. *Journal of the American Ceramic Society*, 56(3):153–157, 1973.

[69] Erik Bitzek, Pekka Koskinen, Franz Gähler, Michael Moseler, and Peter Gumbsch. Structural relaxation made simple. *Physical Review Letters*, 97(17):170201, 2006.

[70] CT Bodur, J Chang, and AS Argon. Molecular dynamics simulations of basal and pyramidal system edge dislocations in sapphire. *Journal of the European Ceramic Society*, 25(8):1431–1439, 2005.

[71] AG Marinopoulos and C Elsässer. Density-functional and shell-model calculations of the energetics of basal-plane stacking faults in sapphire. *Philosophical Magazine Letters*, 81(5):329–338, 2001.

[72] Yinkai Lei, Yu Gong, Zhiyao Duan, and Guofeng Wang. Density functional calculation of activation energies for lattice and grain boundary diffusion in alumina. *Physical Review B*, 87(21):214105, 2013.

[73] JH Gieske and GR Barsch. Pressure dependence of the elastic constants of single crystalline aluminum oxide. *Physica Status Solidi (b)*, 29(1):121–131, 1968.

[74] Nobuo Ishizawa, Tsutomu Miyata, Ichiro Minato, F Marumo, and S Iwai. A structural investigation of α-Al_2O_3 at 2170K. *Acta Crystallographica Section B: Structural Crystallography and Crystal Chemistry*, 36(2):228–230, 1980.

[75] Sandro Jahn, Paul A Madden, and Mark Wilson. Transferable interaction model for Al_2O_3. *Physical Review B*, 74(2):024112, 2006.

[76] Shunli Shang, Yi Wang, and Zi-Kui Liu. First-principles elastic constants of α- and θ-Al_2O_3. *Applied Physics Letters*, 90(10):101909, 2007.

[77] Joanne Sarsam, Michael W Finnis, and Paul Tangney. Atomistic force field for alumina fit to density functional theory. *The Journal of Chemical Physics*, 139(20):204704, 2013.

[78] JR Gladden, Jin H So, JD Maynard, PW Saxe, and Y Le Page. Reconciliation of ab initio theory and experimental elastic properties of Al_2O_3. *Applied Physics Letters*, 85(3):392–394, 2004.

[79] DB Hovis, A Reddy, and AH Heuer. X-ray elastic constants for α-Al_2O_3. *Applied Physics Letters*, 88(13):131910, 2006.

[80] R Tarumi, H Ledbetter, H Ogi, and M Hirao. Low-temperature elastic constants of monocrystal corundum (α-Al_2O_3). *Philosophical Magazine*, 93(36):4532–4543, 2013.

[81] Canan U Hardwicke and Yuk-Chiu Lau. Advances in thermal spray coatings for gas turbines and energy generation: a review. *Journal of Thermal Spray Technology*, 22(5):564–576, 2013.

[82] Wenxu Jia, Yudong Hou, Mupeng Zheng, Yuru Xu, Mankang Zhu, Kuiyong Yang, Huarong Cheng, Shuying Sun, and Jie Xing. Advances in lead-free high-temperature dielectric materials for ceramic capacitor application. *IET Nanodielectrics*, 1(1):3–16, 2018.

[83] Kazumasa Murata, Junya Ohyama, Yuta Yamamoto, Shigeo Arai, and Atsushi Satsuma. Methane combustion over Pd/Al_2O_3 catalysts in the presence of water: effects of Pd particle size and alumina crystalline phase. *ACS Catalysis*, 10(15):8149–8156, 2020.

[84] Arnaud Marmier and Stephen C Parker. Ab initio morphology and surface thermodynamics of α-Al_2O_3. *Physical Review B*, 69(11):115409, 2004.

[85] Jizhong Sun, T Stirner, and A Matthews. Structure and surface energy of low-index surfaces of stoichiometric α-Al_2O_3 and α-Cr_2O_3. *Surface and Coatings Technology*, 201(7):4205–4208, 2006.

[86] P Guenard, G Renaud, A Barbier, and M Gautier-Soyer. Determination of the α-Al_2O_3 (0001) surface relaxation and termination by measurements of crystal truncation rods. *Surface Review and Letters*, 5(01):321–324, 1998.

[87] J Ahn and JW Rabalais. Composition and structure of the Al_2O_3 $\{0001\}$-(1×1) surface. *Surface Science*, 388(1-3):121–131, 1997.

[88] J Toofan and PR Watson. The termination of the α-Al_2O_3 (0001) surface: a LEED crystallography determination. *Surface Science*, 401(2):162–172, 1998.

[89] CF Walters, KF McCarty, EA Soares, and MA Van Hove. The surface structure of α-Al_2O_3 determined by low-energy electron diffraction: aluminum termination and evidence for anomolously large thermal vibrations. *Surface Science*, 464(2-3):L732–L738, 2000.

[90] Takahiro Kurita, Kazuyuki Uchida, and Atsushi Oshiyama. Atomic and electronic structures of α-Al_2O_3 surfaces. *Physical Review B*, 82(15):155319, 2010.

[91] Shiyang Sun, Pingping Xu, Bingyang Ma, Hailong Shang, and Geyang Li. Effects of temperature and O partial pressure on the atomic structure of Al_2O_3 (0001) surface. *Computational Materials Science*, 157:37–42, 2019.

[92] Xiao-Gang Wang, Anne Chaka, and Matthias Scheffler. Effect of the environment on α-Al_2O_3 (0001) surface structures. *Physical Review Letters*, 84(16):3650, 2000.

[93] Alexandra M Goryaeva, Philippe Carrez, and Patrick Cordier. Modeling defects and plasticity in $MgSiO_3$ post-perovskite: Part 1—generalized stacking faults. *Physics and Chemistry of Minerals*, 42(10):781–792, 2015.

[94] Qun Zu, Ya-Fang Guo, and Xiao-Zhi Tang. Analysis on dissociation of pyramidal I dislocation in magnesium by generalized-stacking-fault energy. *Acta Metallurgica Sinica (English Letters)*, 28(7):876–882, 2015.

[95] Binglun Yin, Zhaoxuan Wu, and WA Curtin. Comprehensive first-principles study of stable stacking faults in hcp metals. *Acta Materialia*, 123:223–234, 2017.

[96] PD Tepesch and AA Quong. First-principles calculations of α-alumina (0001) surfaces energies with and without hydrogen. *Physica Status Solidi (B)*, 217(1):377–387, 2000.

[97] Carlo Ruberto, Yashar Yourdshahyan, and Bengt I Lundqvist. Surface properties of metastable alumina: A comparative study of κ- and α-Al_2O_3. *Physical Review B*, 67(19):195412, 2003.

[98] Vaclav Vitek. Intrinsic stacking faults in body-centred cubic crystals. *Philosophical Magazine*, 18(154):773–786, 1968.

[99] Mingwei Chen, En Ma, Kevin J Hemker, Hongwei Sheng, Yinmin Wang, and Xuemei Cheng. Deformation twinning in nanocrystalline aluminum. *Science*, 300(5623):1275–1277, 2003.

[100] Helena Van Swygenhoven, Peter M Derlet, and AG Frøseth. Stacking fault energies and slip in nanocrystalline metals. *Nature Materials*, 3(6):399–403, 2004.

[101] Rudolf Peierls. The size of a dislocation. *Proceedings of the Physical Society (1926-1948)*, 52(1):34, 1940.

[102] FRN Nabarro. Dislocations in a simple cubic lattice. *Proceedings of the Physical Society (1926-1948)*, 59(2):256, 1947.

[103] James R Rice and Robb Thomson. Ductile versus brittle behaviour of crystals. *The Philosophical Magazine: A Journal of Theoretical Experimental and Applied Physics*, 29(1):73–97, 1974.

[104] K Peter D Lagerlöf, Arthur H Heuer, Jacques Castaing, Jean P Rivière, and Terence E Mitchell. Slip and twinning in sapphire (α-al_2o_3). *Journal of the American Ceramic Society*, 77(2):385–397, 1994.

[105] A He, KPD Lagerlöf, J Castaing, and AH Heuer. Considerations of the double-cross-slip mechanism for basal and rhombohedral twinning in sapphire (α-Al_2O_3). *Philosophical Magazine A*, 82(15):2855–2867, 2002.

[106] Emmanuel Clouet, Lisa Ventelon, and François Willaime. Dislocation core energies and core fields from first principles. *Physical Review Letters*, 102(5):055502, 2009.

[107] ML Kronberg. Plastic deformation of single crystals of sapphire: basal slip and twinning. *Acta Metallurgica*, 5(9):507–524, 1957.

[108] AH Heuer. Deformation twinning in corundum. *The Philosophical Magazine: A Journal of Theoretical Experimental and Applied Physics*, 13(122):379–393, 1966.

[109] W D Scott and KK Orr. Rhombohedral twinning in alumina. *Journal of the American Ceramic Society*, 66(1):27–32, 1983.

[110] KPD Lagerlöf, J Castaing, P Pirouz, and AH Heuer. Nucleation and growth of deformation twins: a perspective based on the double-cross-slip mechanism of deformation twinning. *Philosophical Magazine A*, 82(15):2841–2854, 2002.

[111] T Geipel, KPD Lagerlöf, P Pirouz, and AH Heuer. A zonal dislocation mechanism for rhombohedral twinning in sapphire (α-Al_2O_3). *Acta Metallurgica et Materialia*, 42(4):1367–1372, 1994.

[112] Kenji Tsuruta, Eita Tochigi, Yuki Kezuka, Kazuaki Takata, Naoya Shibata, Atsutomo Nakamura, and Yuichi Ikuhara. Core structure and dissociation energetics of basal edge dislocation in α-Al_2O_3: A combined atomistic simulation and transmission electron microscopy analysis. *Acta Materialia*, 65:76–84, 2014.

[113] J Castaing, A He, KPD Lagerlöf, and AH Heuer. Deformation of sapphire (α-Al_2O_3) by basal slip and basal twinning below 700°C. *Philosophical Magazine*, 84(11):1113–1125, 2004.

[114] J Castaing, J Cadoz, and Stephen H Kirby. Prismatic slip of Al_2O_3 single crystals below 1000°C in compression under hydrostatic pressure. *Journal of the American Ceramic Society*, 64(9):504–511, 1981.

[115] Eita Tochigi, Bin Miao, Atsutomo Nakamura, Naoya Shibata, and Yuichi Ikuhara. Atomic-scale mechanism of rhombohedral twinning in sapphire. *Acta Materialia*, 216:117137, 2021.

[116] PA Zhilyaev and AV Yanilkin. Ab initio and classical simulation of the defect formation in sapphire. *Russian Metallurgy (Metally)*, 2012(10):879–883, 2012.

[117] MH Jhon, AM Glaeser, and DC Chrzan. Computational study of stacking faults in sapphire using total energy methods. *Physical Review B*, 71(21):214101, 2005.

[118] Naoya Shibata, MF Chisholm, A Nakamura, SJ Pennycook, T Yamamoto, and Yuichi Ikuhara. Nonstoichiometric dislocation cores in α-alumina. *Science*, 316(5821):82–85, 2007.

[119] J P Hirth and J Lothe. *Theory of dislocations*. John Willey and Sons. John Willey and Sons, 01 1982.